Microstructure and fluid flow in rift border fault-bounded basins – insights from the Dombjerg Fault, NE Greenland

Eric Salomon[1,2,*], Atle Rotevatn[1], Thomas Berg Kristensen[1,3], Sten-Andreas Grundvåg[4], Gijs Allard Henstra[1,5]

[1]Department of Earth Science, University of Bergen, Bergen, Norway

[2]now at GeoZentrum Nordbayern, University of Erlangen-Nuremberg, Erlangen, Germany

[3]now at Equinor ASA, Bergen, Norway

[4]Department of Geosciences, UiT The Arctic University of Norway, Tromsø, Norway

[5]now at AkerBP, Fornebu, Norway

*corresponding author (e.salomon@outlook.de, +49 9131 85 25915)

Abstract

In this contribution, we elucidate the interaction of structural deformation, fluid flow, and diagenesis in hanging wall siliciclastic deposits along rift basin-bounding faults, exemplified at the Dombjerg Fault in NE Greenland. Due to fault-controlled fluid circulation, fault-proximal syn-rift clastic deposits experienced pronounced calcite cementation and became lithified, whereas uncemented clastic deposits remained porous and friable. Correspondingly, two separate deformation regimes developed to accommodate continuous tectonic activity: discrete fractures formed in cemented deposits, and cataclastic deformation bands formed in uncemented deposits.

We show that deformation bands act as partial baffles to fluid flow. This led to localized host rock alteration, which caused a chemical reduction of pore space along the bands. Where cemented, porosity was reduced towards zero and fracture formation created new pathways for fluid migration, which were subsequently filled with calcite. Occasionally, veins comprise multiple generations of microcrystalline calcite, which likely precipitated from an abruptly super-saturated fluid that was injected into the fracture. This suggests that cemented deposits sealed uncemented deposit bodies in which fluid overpressure was able to build up. We conclude that compartmentalized fluid flow regimes may form in rift fault-bounded basins, which has wide implications for assessments of potential carbon storage, hydrocarbon, groundwater, and geothermal sites.

Keywords: syn-rift, fluid flow, fault evolution, structural diagenesis, fracturing, cementation

1. Introduction

Deformation, fluid flow and diagenesis are strongly interactive processes that determine the evolution and properties of clastic sediments and rocks during and following deposition; for example, the style and mechanisms of deformation are highly dependent on the diagenetic state of such host rocks: In unconsolidated and/or poorly lithified, highly porous granular rocks, deformation is commonly accommodated by grain reorganization or crushing that often result in the formation of deformation bands (e.g., Rawling and Goodwin, 2003; Fossen et al., 2018, and references therein). Fluids flow through open pore space in such sedimentary rock and may locally be guided by deformation bands or other heterogeneities such as stratification (e.g., Antonellini and Aydin, 1994, Philipps, 2009). Increasing compaction and cementation leads to a reduction of porosity and permeability (e.g., Lundegard, 1992), while at the same time to an increase of the tensile strength of the rock (e.g., Cook et al., 2015). The latter promotes a transition from granular reorganization and deformation to the formation of discrete fractures, providing new pathways for fluids (e.g., Williams et al., 2017). In turn, pore fluids may, for example, promote cementation, slow the rate of compaction, or be responsible for the creation of secondary porosity, depending on their pressure and composition (e.g., Taylor et al., 2010).

In general, diagenesis of clastic sediments is a function of temperature, burial pressure, and fluid and sediment chemistry (e.g., Worden and Burley, 2003). The presence/development of faults may significantly affect these processes e.g. by influencing heat flow (e.g., Bellani et al., 2004; Townend et al., 2017; Vanneste et al., 2005) and fluid circulation (e.g., Eichhubl and Boles, 2000; Bense et al., 2013; Gibson, 1998). The results of such influence have been showcased along the Dombjerg Fault, a major basin-bounding fault in NE Greenland rift system (Kristensen et al., 2016; Salomon et al., 2020; fig. 1). Here, syn-rift siliciclastic deposits in the hanging wall, juxtaposed against a footwall of crystalline basement, are affected by pervasive fault-proximal calcite cementation, which is interpreted to have resulted from fault-controlled fluid flow and diagenesis.

Previously, Kristensen et al. (2016) have given an overview over the overall structure of the Dombjerg Fault damage zone, and Salomon et al. (2020) analyzed the related fault-controlled diagenetic history and paragenesis. Building on these previous works we here elucidate the effect of this structural and diagenetic evolution on the ensuing fluid flow and deformation history following the establishment of a calcite-cemented zone in the hanging wall of the Dombjerg Fault. The overarching aim of this study is to understand the interaction of deformation, fluid flow and diagenesis operating in the proximity of large, basin-bounding fault systems in rift basins. The work is based on microstructural analyses of the main deformation structures, i.e. veins within the calcite cementation zone, and deformation bands in the uncemented clastic deposits outside the cementation zone. We show that deformation bands acted as local baffles to fluid flow, while cementation created compartments of fluid overpressure that was repeatedly released upon fracturing.

2. Geological Setting

The East Greenland rift system is a long-lived rift system whose formation initiated in the Devonian and which was active episodically throughout Paleozoic and Mesozoic times, until continental breakup and opening of the North Atlantic in the Early Eocene times (e.g., Larsen and Watt, 1985; Surlyk, 1990; Stemmerik et al., 1991; Rotevatn et al., 2018). The rift system is exposed onshore East Greenland along the coast between 68-77°N (Henriksen, 2003; fig. 1a). It is characterized by a right-stepping N-S to NNW-SSE trending border fault network, with segment lengths of 170-230 km (Fig. 1a) and with vertical throws up to ~5 km (Surlyk, 2003).

The Dombjerg Fault is part of this border fault system and marks the western margin of the Wollaston Forland Basin (Fig. 1b). Activity of the fault started in the Carboniferous (Rotevatn et al., 2018) and culminated in a main rift phase in the Late Jurassic / Early Cretaceous (e.g., Surlyk, 1984) at which time the Wollaston Forland Basin was established as a syn-rift half-graben depocentre east of the fault (cf. Gawthorpe and Leeder, 2000). The infill of this half-graben basin can be subdivided into stages of early syn-rift, rift climax, and late syn-rift deposits (sensu Surlyk and Korstgård, 2013; Prosser, 1993). Early syn-rift deposits of Middle to Late Jurassic age are represented by marine sandstones with thin interlayers of mudstone (i.e. Vardekløft and Hall Bredning Groups; fig. 1b; Surlyk and Korstgård, 2013). Rift climax and late syn-rift deposits of Late Jurassic to Early Cretaceous age are assigned to the Wollaston Forland Group, an up to ~3 km thick clastic succession. The lower part of the succession consists predominantly of sandstones and conglomerates that were emplaced by fully submarine gravity flows (Lindemans Bugt Formation; rift climax; Henstra el al., 2016), whereas the succeeding part consists of marine sandstones and conglomerates interfingering with marine mudstones and carbonates (Palnatokes Bjerg Formation; late syn-rift; fig. 1b, Surlyk and Korstgård, 2013).

Of main relevance for this study is the Lindemans Bugt Formation, which forms a clastic wedge that is bounded by the Dombjerg Fault in the west and is gradually thinning eastward into the basin over a distance of 10-15 km (Fig. 1c; Henstra et al., 2016). The deposits of this unit are the erosional products derived from the footwall, which consists for the most part of Caledonian crystalline basement, and were transported as rock falls, debris flows, and turbidity currents into a deep-marine rift basin environment in the hanging wall (Fig. 1; Henstra et al., 2016).

Kristensen et al. (2016) and Salomon et al. (2020) have previously described the diagenetic and deformational character of the rift-climax deep-water clastic deposits of the Lindemans Bugt Formation. We here provide a summary of their main findings as context for the present study. The fault-proximal deposits of the Lindemans Bugt Formation were extensively cemented by calcite within a zone of up to ~1.5 km width into the hanging wall from the fault (Kristensen et al., 2016; Salomon et al., 2020; figs. 2, 3). Close to the fault, cementation is pervasive in the hanging wall deposits, though some beds and intervals remain uncemented (Fig. 3c). Towards the fault-distal margin of the cementation zone, the amount of calcite cement decreases. Here, calcite cement is irregularly distributed within beds, leaving uncemented bodies enclosed by cemented strata (Figs. 3a,b; Salomon et al. 2020). Farther eastward into the basin and outside the cementation zone, calcite cement is confined to selected conglomerate beds only.

Overall, calcite cement pervasively fills intergranular space, which reduces the porosity of the affected deposits towards zero (Salomon et al., 2020) and results in a high competence contrast of the rock relative to the uncemented deposits, which remain porous and friable (Figs. 3a-c). Calcite cementation started shortly after deposition of the clastic sediments during the rift climax in the Valanginian at temperatures between ~30-70°C (Salomon et al., 2020). Calcite veins, which cut through the cemented rock, formed within a similar temperature range, but predominantly in the post-rift phase in the Aptian/Albian (Salomon et al., 2020).

The Dombjerg Fault hanging wall damage zone affects the Lindemans Bugt Formation up to ~500 m into the hanging wall (Kristensen et al., 2016). In fault-proximal outcrops (~100 m from the fault), calcite veins and joints occur at densities of ~7 veins/joints per meter; rarely, minor faults of <10 cm normal displacement are present. Towards the distal parts of the hanging wall damage zone, the vein and joint density decreases to 4 joints/m and 1 calcite vein/m (Kristensen et al., 2016; in the present study, we find similar densities also in outcrops ~1.4 km away from the fault). Joints consistently overprint veins. Where uncemented, the clastic sedimentary rock hosts deformation bands, while veins are absent. These deformation bands occurring outside the cementation zone, and the veins occurring within this zone, form the focus of the present study.

3. Methodology

The study is based on a suite of samples acquired form the Dombjerg Fault hanging wall damage zone during a three-week field season in the summer of 2018. The samples were collected from sedimentary rocks in a transect extending from the fault and up to c. 3.5 km into the hanging wall. The samples comprise veins, deformation bands, and respective wall rocks. In total, we obtained samples for 14 thin sections of calcite veins cutting through cemented sandstones and conglomerates within the cementation zone most proximal to the fault (within c. 1.5 km distance from the fault). Sampling of deformation bands was challenging due to the friable state of the rocks outside the cementation zone; however, a total of 5 thin sections of deformation bands were successfully prepared. Thin sections were analyzed using a Keyence VHX digital optical microscope, a Technosyn 8200Mk II for cold-cathode cathodoluminescence, and Zeiss Supra 55VP and Hitachi TM4000plus scanning electron microscopes for BSE, EDX, and SEM-cathodoluminescence analyses. The two-dimensional porosity of the samples was determined by image analyses of BSE images mosaics using Adobe Photoshop. Previously obtained formation ages and temperatures of calcite veins and cements (based on U-Pb calcite dating and clumped isotope analysis; see Salomon et al., 2020) provide time constraints on the studied cements and vein fills.

4. Results

4.1 Calcite vein characteristics

The cemented deposits are dissected by calcite veins with an overall N-NE trend (Fig. 2), i.e. oblique to the trend of the Dombjerg Fault (NNW-trending; fig. 2). Since most outcrops were exposed in 3-D, we regard this overall trend as unbiased by outcrop orientation. Vein thicknesses range from sub-millimetric to c. 7 cm. All analyzed veins (14 samples) exhibit at least one generation of elongate to blocky syntaxial crystal growth. Separate phases of vein growth are visible in two-thirds of the samples and distinguishable by variable quantities of dust or iron-oxide inclusions (Figs. 4a-d). Crack-seal events are present in 12 of the 14 samples and commonly occur at the contact of vein and wall rock, but occasionally breach through existing vein generations. In all crack-seal events, the younger vein generation does not exceed in thickness the initial vein generation. The majority of veins exhibit opening-mode displacement, while slip zones within the veins are found in three of the 14 samples (Figs. 4g,h).

A distinctively different vein fill is visible in veins of outcrop locations 4 and 17, which appears as an opaque, brownish to greyish calcite matrix that hosts sediment grains (Figs. 3d-g). In thin section view of samples G-9, G-10, G-13 (all from location 4; fig. 2), and G-37 (location 17), this vein fill identifies as multiple generations of microcrystalline calcite with calcite crystal sizes <10 µm that precede the blocky/elongate crystal growth (Figs. 4e,f, 5). In the thin section of sample G-9 (Figs. 3d, 5a-c), taken from a vertical oriented face, the following characteristics stand out:

- A repetitive upward fining of grain size is observable (c.f. point 4 in figure 5b): Quartz, feldspar, and other clasts as well as lithic fragments of cemented wall rock and of earlier vein generations are localized at the bottom in a matrix of microcrystalline calcite. Upward, these components decrease in grain size and mica flakes become the dominant clast type. The remaining upper part of each section consists nearly exclusively of microcrystalline calcite.
- Older vein generations are brecciated, with brecciated fragments consisting of pure microcrystalline calcite or microcrystalline calcite-hosting clasts (c.f. point 2 in figure 5a).
- In at least one generation, mica flakes are aligned parallel to each other with their overall orientation guided by the outline of older vein generations (point 6 in figure 5c).
- In the central section of the vein, a series of thin (<0.5 mm) veins exists with blocky/elongate calcite crystals. These veins align parallel to an anastomosing set of thin (<0.05 mm), dark bands within the microcrystalline calcite (point 5 in figure 5b).

Sample G-37 derives from a fracture, in which the microcrystalline infill is visible from the base of its outcrop exposure upwards over ~50 cm where it is in contact with elongate calcite crystals (Fig. 3g), which fill the remaining upper section of the fracture as far as exposed. In addition, a crack-seal elongate/blocky calcite vein generation has formed along the microcrystalline infill and wall rock (Fig. 3g). In the thin section of sample G-37, multiple generations of upward-fining vein fill are present, similar to the composition and texture in sample G-9 (point 4 in figure 5e). A notable difference to sample G-9 is the absence of crack-seal events with the repeated sealing with microcrystalline calcite. The vein of sample G-13, traceable in the outcrop only on a horizontal surface, comprises a horizontal transition of an elongate calcite vein to microcrystalline calcite hosting sediment grains (Fig. 5).

4.2 Deformation band characteristics

Deformation bands occur in the uncemented deposits outside the cementation zone, and within uncemented bodies of sedimentary rock inside the cementation zone (Figs. 2, 6); deformation bands are absent in the cemented deposits within the cementation zone. The overall trend of the deformation bands is E-NE and thus roughly similar to the orientation of the veins, with the caveat that this observation is based on a limited number of bands (n = 17; fig. 2). In outcrop location 20 (Fig. 2), NE-trending deformation bands cross-cut an older set of NW-trending bands. This NW-trend is also present in a minor set of veins in the nearby location 18 (Fig. 2), although an age relationship between the two vein sets could not be established. One normal fault (Fig. 6f), also NE-trending, was found outside the cementation zone, which is visible in two outcrops ~20 m apart from each other. In one of these, the fault comprises a 25 cm-wide breccia zone (Fig. 6f), while in the second outcrop, this zone is splayed into a ~40 cm-wide cluster of deformation bands (≥ 6 bands), some of which exhibit slickenside surfaces (Fig. 6e). Slickensides indicate normal throw to the NW (see rose plot

Loc. 26 in figure 2). Fault offset clearly exceeds the vertical extent of the outcrop (5 m), as there are distinct marker horizons, but which in the hanging wall are downthrown to below the level of the exposure (samples from this fault are described below).

Deformation band samples are taken from outcrop locations 22 (sample G-48), 23 (samples G-49, G-50), and 26 (samples G-57, G-60), thus from outside the cementation zone (Fig. 2). Samples G-57 and G-60 are derived from the fault described above; G-57 is from the deformation band cluster and G-60 from the center of the breccia zone (Fig. 6f). All deformation bands occur in angular-grained, moderately sorted, fine- to very coarse-grained sub-arkosic sandstone. The fault, represented by sample G-60, also cuts through matrix-supported conglomerate. The sampled bands have an overall strike of E to NE with dip angles between 70-81° (Figs. 6b-f). The amount of offset along the bands could only be determined for samples G-49 and G-50, which exhibit ~5 cm and ~1-2 cm of normal displacement, respectively.

The deformation bands appear slightly variable across the sample suit. Sample G-48 hosts a ~12.5 mm-wide deformation band that, in the thin section, is hard to differentiate from the host rock. The boundary is gradual and the band itself is characterized by a subtle reduction in grain size relative to the host rock, which we attribute to cataclasis (Fig. 7a). The ~15 mm-wide deformation band in sample G-49 has a subtle boundary to the host rock, as well, and hosts a matrix of crushed material and is clast-supported (Fig. 7b). Traces of brownish coloration within the band can be attributed to fragmented biotite flakes. Sample G-50 hosts a ~1.5-3.0 mm-wide deformation band with a boundary to the wall rock that is more distinct, indicated by a strong brown coloration of the wall rock and a band with a high amount of crushed grains forming a matrix-supported structure (Figs. 7c,d). Similar characteristics apply to sample G-57, with the distinction that the thin section hosts an array of three ~2-4 mm wide deformation bands, that are separated by ~2.0-3.5 mm wide zones of compacted wall rock (Figs. 7e,f). G-60 exhibits across the whole thin section intense grain fracturing due to cataclasis, yet a large quantity of intact clasts are present as well (Figs. 7g,h).

4.3 Alteration associated with deformation bands

The sandstone hosting the deformation bands is altered at a varying degree that is expressed in outcrops by a coloration from light grey (seemingly unaltered state) to dark red. While a yellow coloration seems to have formed independently from deformation bands (Figs. 6a,b,f), a red coloration appears to be confined to the bands. Along the band represented by sample G-49 (Fig. 6c), the footwall host rock has a dominant red coloration which is present across the whole length of the footwall's exposure in the outcrop (~5 m). Along the band represented by sample G-57 (Fig. 6e), the red coloration covers a ~5-30 cm wide zone of footwall host rock and fades into a light grey color farther into the footwall, which is also the dominant coloration of the hanging wall. In addition, in the cases of the bands shown in figures 6c and 6d and represented by samples G-49 and G-50, a dark red~1 cm-wide rim occurs along both sides of the bands. In two occasions (Figs. 6c,d), the deformation bands splay and enclose a section of light grey host rock.

While the yellow coloration presumably derives from the alteration of feldspar, the dark red coloration is caused by the precipitation of Fe-/Ti-oxides and jarosite (Fig. 8). Oxides are abundant as rims between the lamellae of biotite flakes and in pore space and grain boundaries surrounding the mica. Jarosite appears as a fine mass in the vicinity to mica flakes although rarely in between mica lamellae (Fig. 8i; EDX spectra and element maps in supplements). A clear age relationship between oxide and jarosite formation could not be established from the thin section analysis. With distance to the deformation band the degree of biotite alteration declines and the presence of oxides and jarosite is commonly confined to parts of expanded/deformed flakes of biotite (Figs. 8f,g). Within the deformation bands, biotite is highly deformed yet unaltered and oxides/jarosite nearly completely absent (Figs. 8b,c).

4.4 Deformation band porosity analysis

We created BSE image mosaics for 2-D porosity image analysis of the five deformation band samples (Fig. 9, table 1). In sample G-48, the wall rock has a porosity of 21.9 % and the deformation band 14.9 %. Sample G-49 yields a wall rock porosity of 18.5 %, a deformation band porosity of 7.1 %, and a porosity in the red-stained zone of 5.2 %. In sample G-50, the wall rock has a porosity of 25.8 %, the deformation band 13.6 %, and the red-stained zone along the band 11.8 %. Sample G-57 hosts three single deformation bands with porosities of 8.0 %, 9.0 %, 9.1 %, respectively, while the slightly reddish altered wall rock has 17.6 % porosity (Fig. 9). Sample G-58, which has been taken ~20 cm away from this band cluster in the more whitish rock (Figs. 6e, 9), the porosity is slightly higher with 21.6 %. We note that all values should only be taken as a rough measure and may be overestimated (e.g., especially sample G-50 suffered from expansion during the epoxy impregnation due to its incohesive condition); however, we are interested in the relative differences rather than the exact values. Summarized, the deformation bands all exhibit lower porosity than their host rocks. Red-stained alteration zones, on the other hand, show somewhat variable porosity.

5. Discussion

5.1 Deformation band structure

Deformation bands are exclusively found in host rocks absent of calcite cement in outcrops both within (in uncemented bodies) and outside the cementation zone; however, no deformation bands are found within cemented deposits, suggesting that the bands likely formed *after* calcite cementation and establishment of the wider cementation zone. We do, for example, not find any deformation bands overprinted by calcite cementation, which further strengthens the hypothesis that calcite cementation pre-dates the formation of deformation bands. Furthermore, the overall orientation of the bands is approximately parallel to the general trend of calcite veins (Fig. 2), which suggests they formed in the same stress system. The majority of veins has been dated to the Aptian/Albian and set in relation to an extension phase from latest Valanginian to middle Albian times (Salomon et al., 2020; see also chapter 5.3).

All sampled deformation bands show a cataclastic reduction of grain size, a mechanism that is seen as the key-controlling factor to reduce porosity and permeability in deformation bands (e.g., Ballas et al., 2015). Compared to the mostly unaltered wall rock, porosity within the deformation bands is reduced by approximately one to two thirds (Fig. 9, table 1), which is well within the range of reported porosity losses from host rock to cataclastic deformation bands elsewhere (e.g., Aydin and Johnson, 1983; Antonellini and Aydin, 1994; Torabi and Fossen, 2009).

5.2 Alteration along deformation bands

At the outcrop scale, three of the analyzed five deformation bands exhibit a control on the degree of host rock alteration. This is indicated by the sharp transition across the band from a yellow/white-colored hanging wall to a red-colored footwall (Figs. 6c,e; represented by samples G-49, G-57) as well as by the unaltered host rock enclosed by splaying deformation bands (Figs. 6c,d; samples G-49, G-50). Such alteration effects along deformation bands have been reported before by others and have been attributed to a control of the bands on local fluid flow (e.g., Exner and Tschegg, 2012; Ballas et al., 2012; Dimmen et al. 2020), and it is widely recognized that deformation bands may act as baffles to flow due to the porosity and permeability reduction in the bands (e.g., Fossen et al., 2007, and references therein).

A clear trend between porosity and degree of host rock alteration is not visible in our dataset. In outcrop location 23, the deformation bands represented by samples G-49 and G-50 yield porosity values of 7.1 % and 13.6 %, respectively. Here, only the low-porosity band of G-50 shows a significant control on footwall alteration (Fig. 6c). Nevertheless, the high-porosity band of G-49 encloses unaltered host rock in a splay zone (Fig. 6d), showcasing the band's potential to also affect host rock alteration. In outcrop location 25, samples G-57 and G-60 derive from the same fault and yield similar porosity values of ~8-9 %, yet alteration only occurs at the site of G-57 (Figs. 6e,f).

Hence, porosity values determined from single samples and the degree of alteration should not immediately be taken as indicators for the bands impact on fluid flow. It has been shown that porosity can be highly variable laterally within a band at a very local scale (Fossen et al., 2018). The degree of cataclasis, i.e. the main contributor to porosity reduction (Fossen et al., 2018), is partially controlled by the host rock composition and texture, e.g. grain sorting, roundness, or mineralogy (e.g., Cheung et al., 2012), which may have had an impact on the analyzed deformation bands. Still, especially the character of the splay zones (Figs. 6c,d) highlight the potential of deformation bands to act as baffles to fluid flow.

Apart from the broader meter-scale control on host rock alteration that dominantly occurs in the footwall, the deformation bands exhibit a control at the cm-scale on alteration on both the hanging wall and footwall sides as indicated by the dark red-stained zones along them (Fig. 6d). As seen in the microscopic analysis, the coloration of this zone is caused by the dominant precipitation of Fe-/Ti-oxides and jarosite. The occurrence of these precipitates along biotite flakes or in their close proximity suggests that they form products of its alteration (Bisdom et al., 1982; Morad, 1990; Li et al., 1998). To a minor degree, jarosite and

Fe-/Ti-oxides occur outside this zone, where they are mostly confined to parts of mica grains where the flakes have been delaminated. This expansion may have resulted from compaction where the mica grains are pressed against adjacent grains and subsequently increased the reaction surface for the mica alteration (Figs. 8f,g).

Deformation bands are commonly surrounded by a thin envelope, i.e. a “transition zone”, where the degree of compaction is slightly higher than the host rock (e.g., Aydin, 1978; Underhill and Woodcock, 1987; Cavailhes and Rotevatn, 2018). Hence, in this zone, biotite should be bent and delaminated to a larger extent providing more reaction surface than in the host rock. Inside the deformation bands, biotite is crushed, however, Fe-/Ti-oxides and jarosite are nearly absent. This may be rooted in the permeability contrast with the deformation band being low-permeable, while in the surrounding transition zone, the pore space is still large enough to allow for fluid flux providing sufficient reactants for biotite alteration. Capillary effects may also favor fluid migration in the transition zone, rather in the host rock (Sigda and Wilson, 2003; Dimmen et al., 2020). The fact that along the bands of samples G-49 and G-50 the red-stained zone occurs on both sides of the band argues for a similar or the same fluid and a similar fluid circulation habit in the footwall and hanging wall of the bands.

5.3 Vein structure

The overall N-NE trend of the veins is oblique to the NW-trending Dombjerg Fault, which may root in the proximity of the outcrop locations to the right-stepping transfer/relay zone between the Dombjerg Fault and the Thomsenland Fault (Figs. 1b, 2). In such a right-stepping setting, local stress perturbation and clockwise re-orientation of the principal stress axes is common (e.g., Çiftçi and Bozkurt, 2007; Rotevatn and Bastesen, 2012; Mercuri et al., 2020), which may explain the overall trend of the veins. However, the setting is complicated by the circumstance that the majority of the veins formed in the post-rift stage in the Aptian/Albian and it is inferred that the vein ages also reflect the time of fracturing (Salomon et al., 2020). Activity of the Dombjerg and Thomsenland faults in the post-rift stage has not been reported of. However, the presence of the transfer zone should still cause local stress perturbations and may therefore influence deformation in response to any regional tectonic activity (e.g., Kattenhorn et al., 2000). Nevertheless, as the vein density increases towards the Dombjerg Fault (Kristensen et al., 2016), activity of the fault does seem feasible.

All veins of the hanging wall show at least one generation of syntaxial growth, which argues for a sudden rather than a creeping fracture opening (e.g., Bons et al., 2012). The series of crack-seal events visible in many veins indicate repetitive opening of the veins, albeit, given the width of the crack-seal generations, these latter fracture openings have never exceeded the initial fracture width. In conjunction with the occurrence of slip zones in some of the veins, this suggests that the initial site of fracturing had been preferential zones of weaknesses susceptible for further fracturing, which is a common observation (e.g., Ramsay, 1980; Petit et al., 1999). The low degree of twinning of the vein calcite indicates that the veins have not been subject to significant deformation or high temperatures after their formation (Burkhard, 1993).

5.4 Microcrystalline calcite

The microcrystalline calcite is an intriguing vein infill that differs significantly from the common elongate/blocky calcite crystal generations. From the observations in thin sections of the microcrystalline calcite-hosting veins (Figs. 4, 5), the following interpretations can be drawn:

- The prominent gradation in many fill generations (Figs. 5a,b,d,e) indicate that the components were in suspension in a fluid before being deposited (e.g., Amy et al., 2006). Microcrystalline calcite was not found as cement in the sandstone, indicating that this calcite precipitated from the fluid in the fracture.
- The aligned generations of microcrystalline calcite parallel to the wall rock in sample G-9 (Fig. 5a) argue for a repetitive fracture opening with repetitive pulses of microcrystalline calcite precipitation. In sample G-37 (Fig. 5d), such alignment is missing, and generations are solely stacked on top of each other. Combined with the horizontal separation of elongate and microcrystalline calcite in vein G-13 (Fig. 5f), this indicates that the amount of microcrystalline calcite can be heterogeneously distributed within a fracture. A reason for this heterogeneity may be a variable fracture aperture and surface roughness of the fracture walls, which generally influence fluid flow velocities and causes non-linear to turbulent flow and may even create eddies (e.g., Wang et al., 2016; Zou et al., 2015). Subsequently, precipitates and particles that are in suspension may settle when being transported into sections of the fracture where low flow velocities prevail.

Microcrystalline calcite is a rather uncommon calcite texture and has rarely been described before in veins (Eichhubl and Boles, 1998, Bishop and Sumner, 2006, and Hendry and Poulsom, 2006, as the only examples known to the authors of this contribution). Commonly, calcite preferably grows on nuclei and existing calcite crystals resulting in the formation of larger crystals (e.g., Bons et al., 2012). We therefore speculate that microcrystalline calcite may have formed in a setting of quick super-saturation that forced a sudden precipitation of calcite from the hosting fluid, preventing an organization of dissolved ions into larger crystals, as similarly proposed for the formation of microcrystalline quartz (Fournier, 1985; Onasch et al., 2010; Shimizu, 2014). A quick super-saturation may be caused by three mechanisms: a sudden pressure drop (e.g., He et al., 1999), a sudden rise of fluid temperature (calcite has a T retrograde solubility; e.g., Plummer and Busenberg, 1982), and fluid mixing (e.g., Tartakovsky et al., 2008).

We regard the influence of temperature as less likely, as we do not identify a heat source that could have caused a sudden local temperature rise. Fluid mixing, which has been considered by Bishop and Sumner (2006), appears plausible in the setting along the Dombjerg Fault, as a fluid in uncemented sediment enclosed by the cementation zone may have a different composition than a fluid outside the cementation zone. Fracturing of cemented layers may connect and mix these fluids causing calcite precipitation within the fracture. This may explain the occurrence of microcrystalline calcite only in fractures. After some time, fluids may reach equilibrium and calcite precipitation continues at a slower rate under normal advective conditions.

Pressure drop has been proposed by Eichhubl and Boles (1998) that follows a previous build-up of CO_2 partial pressure (pCO_2) in the fluid. CO_2 is produced by a number of degradation processes of organic material, e.g. during bacterial sulfate reduction (e.g., Baumgartner et al., 2006). Along the Dombjerg Fault, this process is regarded as responsible for the supply of carbon for calcite cement and veins (Salomon et al., 2020). It may be feasible, that pCO_2 was able to build up in uncemented bodies and layers enclosed and sealed off by the cementation zone. In addition, progressive burial would generally increase the fluid pressure in these bodies as the uncemented porous deposits are susceptible to mechanical compaction (e.g., Paxton et al., 2002). If the sealing cemented layer covering the uncemented bodies is breached by a fracture, the overpressured fluid would inject into the fracture and be subject to a sudden pressure drop within the fracture (Sibson et al., 1988). In addition, the fracture should act as a Venturi conduit in which fluid pressure is lower than upstream and downstream of the fracture (e.g., Furbish, 1997; Zhang, 2017). Both mechanisms favor sudden super-saturation within the fracture, leading to quick precipitation of calcite; they may also serve as an explanation for the preferred occurrence of microcrystalline calcite in the fracture and its absence in the pore space of the surrounding host rocks.

Following this argumentation, the energy of the injected fluid would be sufficiently large to carry sediment grains from the uncemented bodies into the fracture and to brecciate older generations of microcrystalline calcite in the vein (see figure 10 for a conceptual evolutionary model). Grains may have also trickled down into the fracture from a potentially overlying uncemented sediment bed or derived from the immediate cemented wall rocks. The latter seems less likely as a significant contributor though, as the fracture walls are rather smooth with cut-off grains, and there is no evidence to support grain fall-out from fracture wall, apart from larger rock fragments. Fluid flow within a fracture is often non-linear and may even be turbulent (e.g., Wang et al., 2016; Zou et al., 2015) giving rise to an unequal deposition of grains, rock fragments and precipitating microcrystalline calcite within the fracture (Fig. 10c). The existence of multiple fracture fill generations indicates a cyclicity in their formation. The settling of microcrystalline calcite from suspension may seal the fracture allowing a renewed buildup of fluid pressure in the underlying sediment. Hydraulic (Fig. 10c) or tectonic (Fig. 10d) fracturing would allow the repetitive injection of fluid into the fracture with the corresponding pressure release and microcrystalline calcite precipitation.

6. Conclusions

Activity of the Dombjerg Fault and the connected formation of a cementation zone in its proximity has created an environment that showcases the interaction of sediment diagenesis, tectonic-controlled deformation, and fluid chemistry and flow in clastic rocks along rift-bounded fault systems:

- Uncemented, poorly lithified porous clastic deposits are susceptible to the formation of deformation bands and accompanied localized host rock alterations, forming partial baffles to fluid flow.
- Fault-controlled fluid circulation may lead to extensive calcite (or other) cementation of hanging-wall clastic deposits along basin bounding fault systems in rift basins, reducing primary pore space towards zero (cf. Salomon et al., 2020). Where cemented, the clastic deposits may be susceptible to fracturing, forming secondary porosity and new pathways for fluids.
- Cemented sediment bodies have the capacity to seal uncemented compartments, which may become subject to fluid overpressure during increasing burial. Cyclic (hydro-)fracturing repeatedly releases this pressure.

These observations highlight how a calcite cementation zone is able to compartmentalize a syn-rift sedimentary basin into a pore- and a fracture-controlled fluid flow regime. This has important implications for the assessment and planning of potential CO_2 storage, hydrocarbon exploration and production, groundwater aquifers, and geothermal sites (e.g., placement of well sites). It demonstrates the significance of understanding the interplay between diagenesis, deformation and fluid flow during the evolution of fault-bounded basins.

Acknowledgments

Arild Andresen is thanked for giving support in planning and providing equipment for the field campaign. The Ministry of Environment and Nature and the Mineral License and Safety Authority of the government of Greenland are thanked for allowing access to the Northeast Greenland National Park for fieldwork conducted under KNNO expedition permit C-18-56 and Scientific Survey License VU-00141. Daniel Koehn and Matteo Demurtas are thanked for helpful discussions. This research was conducted as part of the ARCEx project and has been supported by the Research Council of Norway (grant no. 228107).

References

Amy, L.A., Talling, P.J., Edmonds, V.O., Sumner, E.J., Lesueur, A., 2006. An experimental investigation of sand?mud suspension settling behaviour: implications for bimodal mud contents of submarine flow deposits. Sedimentology 53, 1411–1434. https://doi.org/10.1111/j.1365-3091.2006.00815.x.

Antonellini, M., Aydin, A., 1994. Effect of Faulting on Fluid Flow in Porous Sandstones: Petrophysical Properties. Bulletin 78. https://doi.org/10.1306/BDFF90AA-1718-11D7-8645000102C1865D.

Aydin, A., 1978. Small Faults Formed as Deformation Bands in Sandstone, in: Rock Friction and Earthquake Prediction. Birkhäuser, Basel, pp. 913–930.

Aydin, A., Johnson, A.M., 1983. Analysis of faulting in porous sandstones. Journal of Structural Geology 5, 19–31. https://doi.org/10.1016/0191-8141(83)90004-4.

Ballas, G., Fossen, H., Soliva, R., 2015. Factors controlling permeability of cataclastic deformation bands and faults in porous sandstone reservoirs. Journal of Structural Geology 76, 1–21. https://doi.org/10.1016/j.jsg.2015.03.013.

Ballas, G., Soliva, R., Sizun, J.-P., Benedicto, A., Cavailhes, T., Raynaud, S., 2012. The importance of the degree of cataclasis in shear bands for fluid flow in porous sandstone, Provence, FranceCataclastic Shear Bands and Fluid Flow in Porous Sandstone. AAPG Bulletin 96, 2167–2186. https://doi.org/10.1306/04051211097.

Baumgartner, L.K., Reid, R.P., Dupraz, C., Decho, A.W., Buckley, D.H., Spear, J.R., Przekop, K.M., Visscher, P.T., 2006. Sulfate reducing bacteria in microbial mats: Changing paradigms, new discoveries. Sedimentary Geology 185, 131–145. https://doi.org/10.1016/j.sedgeo.2005.12.008.

Bellani, S., Brogi, A., Lazzarotto, A., Liotta, D., Ranalli, G., 2004. Heat flow, deep temperatures and extensional structures in the Larderello Geothermal Field (Italy): constraints on geothermal fluid flow. Journal of Volcanology and Geothermal Research 132, 15–29. https://doi.org/10.1016/S0377-0273(03)00418-9.

Bense, V.F., Gleeson, T., Loveless, S.E., Bour, O., Scibek, J., 2013. Fault zone hydrogeology. Earth-Science Reviews 127, 171–192. https://doi.org/10.1016/j.earscirev.2013.09.008.

Bisdom, E.B.A., Stoops, G., Delvigne, J., Curmi, P., Altemuller, H.-J., 1982. Micromorphology of weathering biotite and its secondary products. Pedologie, 225–252.

Bishop, J.W., Sumner, D.Y., 2006. Molar tooth structures of the Neoarchean Monteville Formation, Transvaal Supergroup, South Africa. I: Constraints on microcrystalline CaCO3 precipitation. Sedimentology 53, 1049–1068. https://doi.org/10.1111/j.1365-3091.2006.00801.x.

Bons, P.D., Elburg, M.A., Gomez-Rivas, E., 2012. A review of the formation of tectonic veins and their microstructures. Journal of Structural Geology 43, 33–62. https://doi.org/10.1016/j.jsg.2012.07.005.

Burkhard, M., 1993. Calcite twins, their geometry, appearance and significance as stress-strain markers and indicators of tectonic regime: a review. Journal of Structural Geology 15, 351–368. https://doi.org/10.1016/0191-8141(93)90132-t.

Burley, S.D., Worden, R.H. (Eds.), 2003. Sandstone diagenesis: Recent and ancient. Blackwell, [Oxford], 1 livre électronique (e-book).

Cavailhes, T., Rotevatn, A., 2018. Deformation bands in volcaniclastic rocks – Insights from the Shihtiping tuffs, Coastal Range of Taiwan. Journal of Structural Geology 113, 155–175. https://doi.org/10.1016/j.jsg.2018.06.004.

Cheung, C.S.N., Baud, P., Wong, T.-f., 2012. Effect of grain size distribution on the development of compaction localization in porous sandstone. Geophysical Research Letters 39. https://doi.org/10.1029/2012GL053739.

Çiftçi, N.B., Bozkurt, E., 2007. Anomalous stress field and active breaching at relay ramps: a field example from Gediz Graben, SW Turkey. Geological Magazine 144, 687–699. https://doi.org/10.1017/S0016756807003500.

Cook, J.E., Goodwin, L.B., Boutt, D.F., Tobin, H.J., 2015. The effect of systematic diagenetic changes on the mechanical behavior of a quartz-cemented sandstone. Bulletin 80, D145-D160. https://doi.org/10.1190/geo2014-0026.1.

Dimmen, V., Rotevatn, A., Nixon, C.W., 2020. The Relationship between Fluid Flow, Structures, and Depositional Architecture in Sedimentary Rocks: An Example-Based Overview. Geofluids 2020. https://doi.org/10.1155/2020/3506743.

Eichhubl, P., Boles, J.R., 1998. Vein formation in relation to burial diagenesis in the Miocene Monterey Formation, Arroyo Burro beach, Santa Barbara, California. Pacific Section SEPM Special Publication, 15–36.

Eichhubl, P., Boles, J.R., 2000. Focused fluid flow along faults in the Monterey Formation, coastal California. Geological Society of America Bulletin 112, 1667–1679. https://doi.org/10.1130/0016-7606(2000)112<1667:FFFAFI>2.0.CO;2.

Exner, U., Tschegg, C., 2012. Preferential cataclastic grain size reduction of feldspar in deformation bands in poorly consolidated arkosic sands. Journal of Structural Geology 43, 63–72. https://doi.org/10.1016/j.jsg.2012.08.005.

Fossen, H., Schultz, R.A., Shipton, Z.K., Mair, K., 2007. Deformation bands in sandstone: a review. Journal of the Geological Society 164, 755–769. https://doi.org/10.1144/0016-76492006-036.

Fossen, H., Soliva, R., Ballas, G., Trzaskos, B., Cavalcante, C., Schultz, R.A., 2018. A review of deformation bands in reservoir sandstones: geometries, mechanisms and distribution. Geological Society, London, Special Publications 459, 9–33. https://doi.org/10.1144/SP459.4.

Fournier, R.O., 1985. The behavior of silica in hydrothermal solutions. Review in Economic Geology 2, 45–60.

Furbish, D.J., 1997. Fluid Physics in Geology: An Introduction to Fluid Motions on Earth's Surface and within Its Crust. Oxford University Press.

Gawthorpe, R.L., Leeder, M.R., 2000. Tectono-sedimentary evolution of active extensional basins. Basin Research 12, 195–218. https://doi.org/10.1046/j.1365-2117.2000.00121.x.

Gibson, R.G., 1998. Physical character and fluid-flow properties of sandstone-derived fault zones. Geological Society, London, Special Publications 127, 83–97. https://doi.org/10.1144/GSL.SP.1998.127.01.07.

He, S., Kan, A.T., Tomson, M.B., 1999. Inhibition of calcium carbonate precipitation in NaCl brines from 25 to 90°C. Applied Geochemistry 14, 17–25. https://doi.org/10.1016/S0883-2927(98)00033-X.

Hendry, J.P., Poulsom, A.J., 2006. Sandstone-hosted concretions record evidence for syn-lithification seismicity, cavitation processes, and Palaeocene rapid burial of Lower Cretaceous deep-marine sandstones (Outer Moray Firth, UK North Sea). Journal of the Geological Society 163, 447–460. https://doi.org/10.1144/0016-764905-033.

Henriksen, N., 2003: Caledonian Orogen East Greenland 70–82∘ N, Geological map 1:100 000, Tech. rep., GEUS, Copenhagen, Greenland, p. 1.

Henstra, G.A., Grundvåg, S.-A., Johannessen, E.P., Kristensen, T.B., Midtkandal, I., Nystuen, J.P., Rotevatn, A., Surlyk, F., Sæther, T., Windelstad, J., 2016. Depositional processes and stratigraphic architecture within a coarse-grained rift-margin turbidite system: The Wollaston Forland Group, east Greenland. Marine and Petroleum Geology 76, 187–209. https://doi.org/10.1016/j.marpetgeo.2016.05.018.

Kattenhorn, S.A., Aydin, A., Pollard, D.D., 2000. Joints at high angles to normal fault strike: an explanation using 3-D numerical models of fault-perturbed stress fields. Journal of Structural Geology 22, 1–23. https://doi.org/10.1016/s0191-8141(99)00130-3.

Kristensen, T.B., Rotevatn, A., Peacock, D.C.P., Henstra, G.A., Midtkandal, I., Grundvåg, S.-A., 2016. Structure and flow properties of syn-rift border faults: The interplay between fault damage and fault-related chemical alteration (Dombjerg Fault, Wollaston Forland, NE Greenland). Journal of Structural Geology 92, 99–115. https://doi.org/10.1016/j.jsg.2016.09.012.

Larsen, L.M., Watt, W.S., 1985. Episodic volcanism during break-up of the North Atlantic: evidence from the East Greenland plateau basalts. Earth and Planetary Science Letters 73, 105–116. https://doi.org/10.1016/0012-821X(85)90038-X.

Li, G., Peacor, D.R., Essene, E.J., 1998. The Formation of Sulfides During Alteration of Biotite to Chlorite-Corrensite. Clays Clay Miner. 46, 649–657. https://doi.org/10.1346/CCMN.1998.0460605.

Lundegard, P.D., 1992. Sandstone porosity loss; a "big picture" view of the importance of compaction. Journal of Sedimentary Research 62, 250–260. https://doi.org/10.1306/D42678D4-2B26-11D7-8648000102C1865D.

Mercuri, M., McCaffrey, K.J.W., Smeraglia, L., Mazzanti, P., Collettini, C., Carminati, E., 2020. Complex geometry and kinematics of subsidiary faults within a carbonate-hosted relay ramp. Journal of Structural Geology 130, 103915. https://doi.org/10.1016/j.jsg.2019.103915.

Onasch, C.M., Farver, J.R., Dunne, W.M., 2010. The role of dilation and cementation in the formation of cataclasite in low temperature deformation of well cemented quartz-rich rocks. Journal of Structural Geology 32, 1912–1922. https://doi.org/10.1016/j.jsg.2010.04.013.

Paxton, S.T., Szabo, J.O., Ajdukiewicz, J.M., Klimentidis, R.E., 2002. Construction of an Intergranular Volume Compaction Curve for Evaluating and Predicting Compaction and Porosity Loss in Rigid-Grain Sandstone Reservoirs. AAPG Bulletin 86, 2047–2067. https://doi.org/10.1306/61EEDDFA-173E-11D7-8645000102C1865D.

Petit, J.-P., Wibberley, C.A.J., Ruiz, G., 1999. `Crack–seal', slip: a new fault valve mechanism? Journal of Structural Geology 21, 1199–1207. https://doi.org/10.1016/s0191-8141(99)00038-3.

Phillips, O.M., 2009. Geological Fluid Dynamics. Cambridge University Press, Cambridge.

Prosser, S., 1993. Rift-related linked depositional systems and their seismic expression. Geological Society, London, Special Publications 71, 35–66. https://doi.org/10.1144/GSL.SP.1993.071.01.03.

Ramsay, J.G., 1980. The crack–seal mechanism of rock deformation. Nature 284, 135–139. https://doi.org/10.1038/284135a0.

Rawling, G.C., Goodwin, L.B., 2003. Cataclasis and particulate flow in faulted, poorly lithified sediments. Journal of Structural Geology 25, 317–331. https://doi.org/10.1016/S0191-8141(02)00041-X.

Rotevatn, A., Bastesen, E., 2014. Fault linkage and damage zone architecture in tight carbonate rocks in the Suez Rift (Egypt): implications for permeability structure along segmented normal faults. Geological Society, London, Special Publications 374, 79–95. https://doi.org/10.1144/SP374.12.

Rotevatn, A., Kristensen, T.B., Ksienzyk, A.K., Wemmer, K., Henstra, G.A., Midtkandal, I., Grundvåg, S.-A., Andresen, A., 2018. Structural Inheritance and Rapid Rift-Length Establishment in a Multiphase Rift: The East Greenland Rift System and its Caledonian Orogenic Ancestry. Tectonics 37, 1858–1875. https://doi.org/10.1029/2018TC005018.

Sadoon Morad, 1990. Mica Alteration Reactions in Jurassic Reservoir Sandstones from the Haltenbanken Area, Offshore Norway. Clays Clay Miner. 38, 584–590. https://doi.org/10.1346/CCMN.1990.0380603.

Salomon, E., Rotevatn, A., Kristensen, T.B., Grundvåg, S.-A., Henstra, G.A., Meckler, A.N., Albert, R., Gerdes, A., 2020. Fault-controlled fluid circulation and diagenesis along basin-bounding fault systems in rifts - insights from the East Greenland rift system. Solid Earth 11, 1987–2013. https://doi.org/10.5194/se-11-1987-2020.

Shimizu, T., 2014. Reinterpretation of Quartz Textures in Terms of Hydrothermal Fluid Evolution at the Koryu Au-Ag Deposit, Japan. Economic Geology 109, 2051–2065. https://doi.org/10.2113/econgeo.109.7.2051.

Sibson, R.H., Robert, F., Poulsen, K.H., 1988. High-angle reverse faults, fluid-pressure cycling, and mesothermal gold-quartz deposits. Geology 16, 551–555. https://doi.org/10.1130/0091-7613(1988)016<0551:HARFFP>2.3.CO;2.

Sigda, J.M., Wilson, J.L., 2003. Are faults preferential flow paths through semiarid and arid vadose zones? Water Resources Research 39. https://doi.org/10.1029/2002WR001406.

Stemmerik, L., Vigran, J.O., Piasecki, S., 1991. Dating of late Paleozoic rifting events in the North Atlantic: New biostratigraphic data from the uppermost Devonian and Carboniferous of East Greenland. Geol 19, 218. https://doi.org/10.1130/0091-7613(1991)019<0218:DOLPRE>2.3.CO;2.

Surlyk, F., 1984. Fan-Delta to Submarine Fan Conglomerates of the Volgian-Valanginian Wollaston Forland Group, East Greenland. Canadian Society of Petroleum Geology, 359–382.

Surlyk, F., 1990. Timing, style and sedimentary evolution of Late Palaeozoic-Mesozoic extensional basins of East Greenland. Geological Society, London, Special Publications 55, 107–125. https://doi.org/10.1144/GSL.SP.1990.055.01.05.

Surlyk, F., 2003. The Jurassic of Denmark and Greenland: The Jurassic of East Greenland: a sedimentary record of thermal subsidence, onset and culmination of rifting. Geological Survey of Denmark and Greenland Bulletin, 1, 659–722

Surlyk, F., Korstgård, J., 2013. Crestal unconformities on an exposed Jurassic tilted fault block, Wollaston Forland, East Greenland as an analogue for buried hydrocarbon traps. Marine and Petroleum Geology 44, 82–95. https://doi.org/10.1016/j.marpetgeo.2013.03.009.

Tartakovsky, A.M., Redden, G., P. C. Lichtner, P. C., T. D. Scheibe, T. D., Meakin, P., 2008. Mixing-induced precipitation: Experimental study and multiscale numerical analysis. Water Resources Research 44. https://doi.org/10.1029/2006WR005725.

Taylor, T.R., Giles, M.R., Hathon, L.A., Diggs, T.N., Braunsdorf, N.R., Birbiglia, G.V., Kittridge, M.G., Macaulay, C.I., Espejo, I.S., 2010. Sandstone diagenesis and reservoir quality prediction: Models, myths, and reality. AAPG Bulletin 94, 1093–1132. https://doi.org/10.1306/04211009123.

Torabi, A., Fossen, H., 2009. Spatial variation of microstructure and petrophysical properties along deformation bands in reservoir sandstones. AAPG Bulletin 93, 919–938. https://doi.org/10.1306/03270908161.

Townend, J., Sutherland, R., Toy, V.G., Doan, M.-L., Célérier, B., Massiot, C., Coussens, J., Jeppson, T., Janku-Capova, L., Remaud, L., Upton, P., Schmitt, D.R., Pezard, P., Williams, J., Allen, M.J., Baratin, L.-M., Barth, N., Becroft, L., Boese, C.M., Boulton, C., Broderick, N., Carpenter, B., Chamberlain, C.J., Cooper, A., Coutts, A., Cox, S.C., Craw, L., Eccles, J.D., Faulkner, D., Grieve, J., Grochowski, J., Gulley, A., Hartog, A., Henry, G., Howarth, J., Jacobs, K., Kato, N., Keys, S., Kirilova, M., Kometani, Y., Langridge, R., Lin, W., Little, T., Lukacs, A., Mallyon, D., Mariani, E., Mathewson, L., Melosh, B., Menzies, C., Moore, J., Morales, L., Mori, H., Niemeijer, A., Nishikawa, O., Nitsch, O., Paris, J., Prior, D.J., Sauer, K., Savage, M.K., Schleicher, A., Shigematsu, N., Taylor-Offord, S., Teagle, D., Tobin, H., Valdez, R., Weaver, K., Wiersberg, T., Zimmer, M., 2017. Petrophysical, Geochemical, and Hydrological Evidence for Extensive Fracture-Mediated Fluid and Heat Transport in the Alpine Fault's Hanging-Wall Damage Zone. Geochem. Geophys. Geosyst. 18, 4709–4732. https://doi.org/10.1002/2017GC007202.

Underhill, J.R., Woodcock, N.H., 1987. Faulting mechanisms in high-porosity sandstones; New Red Sandstone, Arran, Scotland. Geological Society, London, Special Publications 29, 91–105. https://doi.org/10.1144/GSL.SP.1987.029.01.09.

Vanneste, M., Guidard, S., Mienert, J., 2005. Bottom-simulating reflections and geothermal gradients across the western Svalbard margin. Terra Nova 17, 510–516. https://doi.org/10.1111/j.1365-3121.2005.00643.x.

Wang, M., Chen, Y.-F., Ma, G.-W., Zhou, J.-Q., Zhou, C.-B., 2016. Influence of surface roughness on nonlinear flow behaviors in 3D self-affine rough fractures: Lattice Boltzmann simulations. Advances in Water Resources 96, 373–388. https://doi.org/10.1016/j.advwatres.2016.08.006.

Williams, R.T., Goodwin, L.B., Mozley, P.S., 2017. Diagenetic controls on the evolution of fault-zone architecture and permeability structure: Implications for episodicity of fault-zone fluid transport in extensional basins. Geological Society of America Bulletin 129, 464–478. https://doi.org/10.1130/B31443.1.

Worden, R.H., Burley, S.D., 2003. Sandstone Diagenesis: The Evolution of Sand to Stone, in: Burley, S.D., Worden, R.H. (Eds.), Sandstone diagenesis: Recent and ancient. Blackwell, [Oxford], pp. 1–44.

Zhang, J.X., 2017. Analysis on the effect of venturi tube structural parameters on fluid flow. AIP Advances 7, 65315. https://doi.org/10.1063/1.4991441.

Zou, L., Jing, L., Cvetkovic, V., 2015. Roughness decomposition and nonlinear fluid flow in a single rock fracture. International Journal of Rock Mechanics and Mining Sciences 75, 102–118. https://doi.org/10.1016/j.ijrmms.2015.01.016.

Figure Captions

Figure 1: (a) Regional geological map of NE Greenland with right-stepping rift boundary fault system separating Devonian-Jurassic sedimentary basins from Caledonian basement. (b) Geological map of the Wollaston Forland and its surrounding. (c) Geological cross section of the Wollaston Forland Basin (see (b) for location). Modified after Rotevatn et al. (2018), based on Surlyk et al. (1993), Surlyk (2003), Henriksen (2003), Surlyk and Korstgård (2013), and Henstra et al. (2016).

Figure 2: Geological map of study area with locations of outcrops and samples analyzed in this study. Inset of stereographic plot shows orientation of calcite veins / deformation bands in the respective outcrops. Sample coordinates provided in supplementary table S1. See Fig. 1b for location. Base satellite image from Google Earth / Digital Globe.

Figure 3: Field photos illustrating characteristics of veins and contact of cemented and uncemented sediments. (a,b) calcite cementation form lobes and appears to partially enclose uncemented sediments; (c) single sediment layers and lenses (light yellowish color) remain devoid of calcite cement in otherwise dominant calcite-cemented strata; (d) vein fill consisting of multiple generations of microcrystalline calcite (location of sample G-9 thin section marked with white frame); (e) calcite vein with a thin rim of microcystalline calcite (sample G-10 derives from this vein, though exact location not in picture); (f) vein consisting of a microcrystalline calcite rim and an infill of microcrystalline calcite and sediment grains (sample G-13 derives from this vein, though exact location not in picture); (g) microcrystalline calcite infill succeeded by elongate calcite growth in upper part of vein (location of sample G-37 thin section marked with white frame). See figure 2 for location of photos.

Figure 4: Thin section photos of calcite veins. (a,b) vein with growth generations that are distinguishable through the degree of dust inclusions; (c,d) vein exhibiting growth zonations with the inclusion of Fe-oxide precipitates; (e,f) vein exhibiting crack-seal texture with inclusion bands; light brownish material is microcystalline calcite (see chapter 4.2 and figure 5 for detailed explanations); (g,h) vein comprising multiple fault slip zones. All images taken in polarized incident ring light.

Figure 5: Thin section photos of three vein samples hosting microcystalline calcite (MC; light brownish mass in cross-polarized light) infill. (a-c) vertical face of sample G-9 shows an array of vein fill generations parallel to the wall rock. Within the generations a repeated gradation of upward fining infill is present. (d, e) vertical face of sample G-37 exhibits multiple generations of upward-fining vein fill, that are succeeded by elongate calcite crystal growth. (f) the horizontal face of sample G-13 shows a transition of vein fill from

elongate calcite crystals to MC hosting lithic fragments. Main characteristics in thin sections are pointed out with numbers.

Figure 6: Field photos of deformation bands with orientation and sample position (where available). (a) deformation band offsetting a layer of organic material by ~3 cm normally (apparent reverse displacement is due to cutting effect; location 20). (b) deformation band with no visible offset (location 22). (c) deformation band with ~5 cm normal displacement and exhibiting a splay zone enclosing a section of unaltered host rock; note the preferred reddish alteration of the footwall (location 23). (d) deformation band splay enclosing unaltered host rock; note dark reddish rim along band in the otherwise yellowish host rock (location 23); (e) deformation band showcasing dominant footwall alteration, while hanging wall rock remains unaltered. (f) deformation band cluster that has merged to form a mature fault with an offset >5 m (i.e. larger than exposed vertical section). Note that structures in (e) and (f) are taken ~20 m apart from each other and derive from the same fault (location 26).

Figure 7: Thin section photos of deformation bands. (a,b) samples G-48 and G-49 comprise deformation bands with low degree of cataclasis and subtle boundary to wall rock. (c,d) sample G-50 with deformation band showing a distinct boundary to the wall rock indicated by the brownish coloration of the latter; (e,f) sample G-57 exhibiting an array of three deformation bands; (g,h) sample G-60, deriving from the core of a cataclastic zone (figure 6f) showing intense grain fracturing and cataclasis in the whole thin section. Images a,c,e,g are taken in polarized incident ring light; d,h in plane-polarized light; f in backscattered electron. Large pores in all images are due to grain plucking during thin section preparation. For locations of samples in the outcrop see figure 6.

Figure 8: Thin section photos of deformation band and wall rock illustrating the degree of biotite alteration (a-g of sample G-50; h, i of sample G-57) in plane polarized light

and backscatter electron imaging in and along the deformation band. (b,c) unaltered and intensively deformed biotite within deformation band; (d,e) altered and deformed and broken biotite lamellae with large quantity of Fe-oxides in red-stained zone; (f,g) slightly deformed biotite with alteration and oxide-precipitation restricted to delaminated part of biotite grain in wall rock; (h,i) intense oxide and pyrite precipitation within and near biotite grains in sample G-57 (EDX spectra and element maps in supplements S2).

Figure 9: Thin section photos of deformation bands (sample G-50, G-57) and host rock (sample G-58) with respective porosity values. Notice the porosity reduction from host rock to bands resulting from the cataclastic grain crushing. Porosity reduction also occurs along the bands, due to preferential precipitation of Fe- / Ti- oxides and pyrite (sample G-50). Sample G-58 is taken ~20 cm away from sample G-57 and has a porosity slightly higher than the host rock of G-57. This is in agreement with field appearance with a decrease in red staining away from the cluster of deformation bands. Porosity derived from 2-D image analysis of backscatter electron images (inset overlays in images).

Figure 10: Conceptual model for the formation of microcrystalline calcite infill found in number of veins cutting through cemented sandstone within the cementation zone along the Dombjerg Fault. The inferred main driver for the formation is initial calcite-saturated overpressured fluid in uncemented sandstone whose injection into a forming fracture is accompanied by sudden fluid pressure drop. This results in an instant super-saturation with respect to calcite and forces its quick precipitation.

Table Captions

Table 1: Porosity data of deformation band samples derived from BSE image analysis (cf. fig. 9).

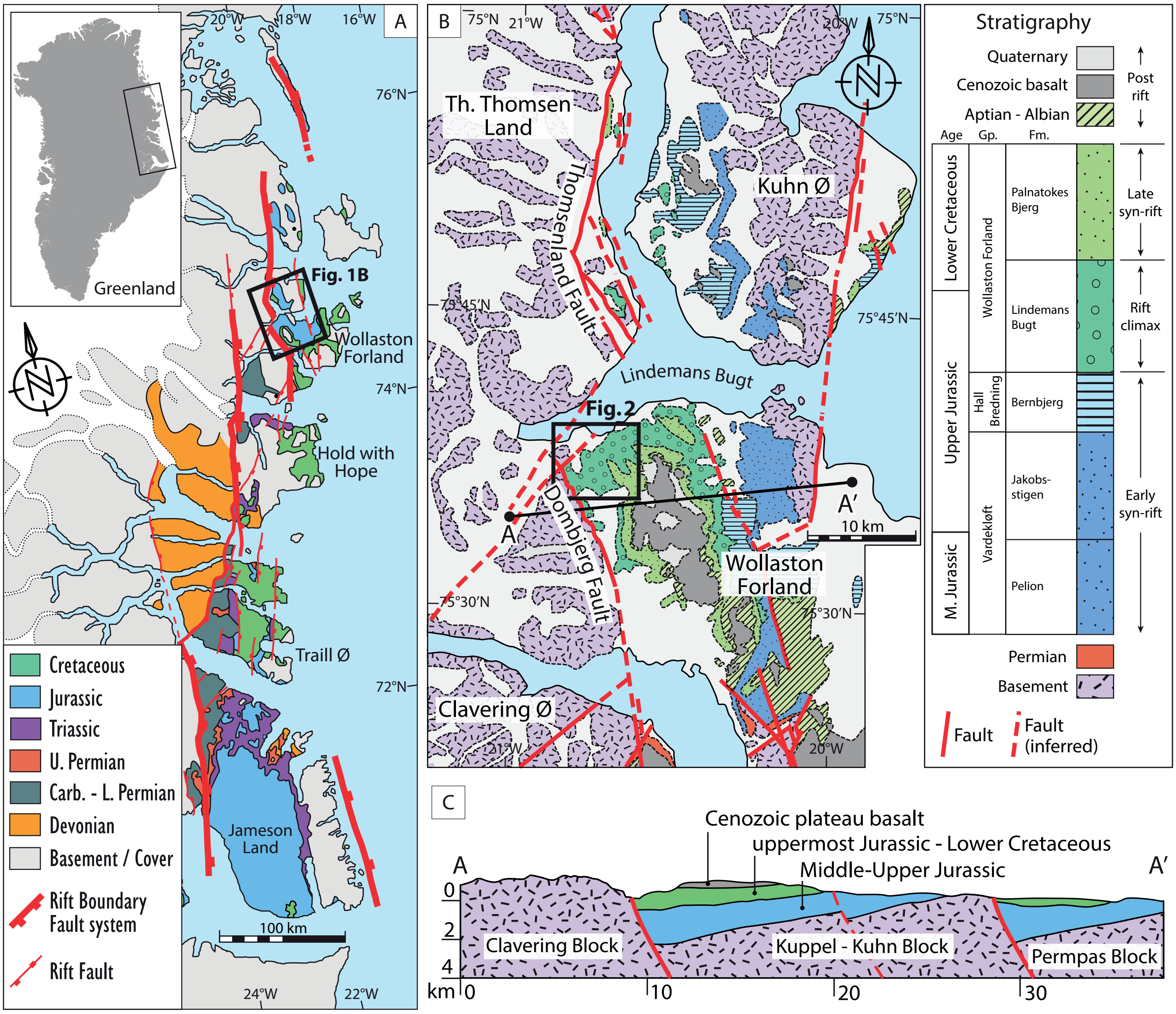

Figure 1. (a) Regional geological map of NE Greenland with right-stepping rift boundary fault system separating Devonian-Jurassic sedimentary basins from Caledonian basement. (b) Geological map of the Wollaston Forland and its surrounding. (c) Geological cross section of the Wollaston Forland Basin (see (b) for location). Modied after Rotevatn et al. (2018), based on Surlyk et al. (1993), Surlyk (2003), Henriksen (2003), Surlyk and Korstgård (2013), and Henstra et al. (2016).

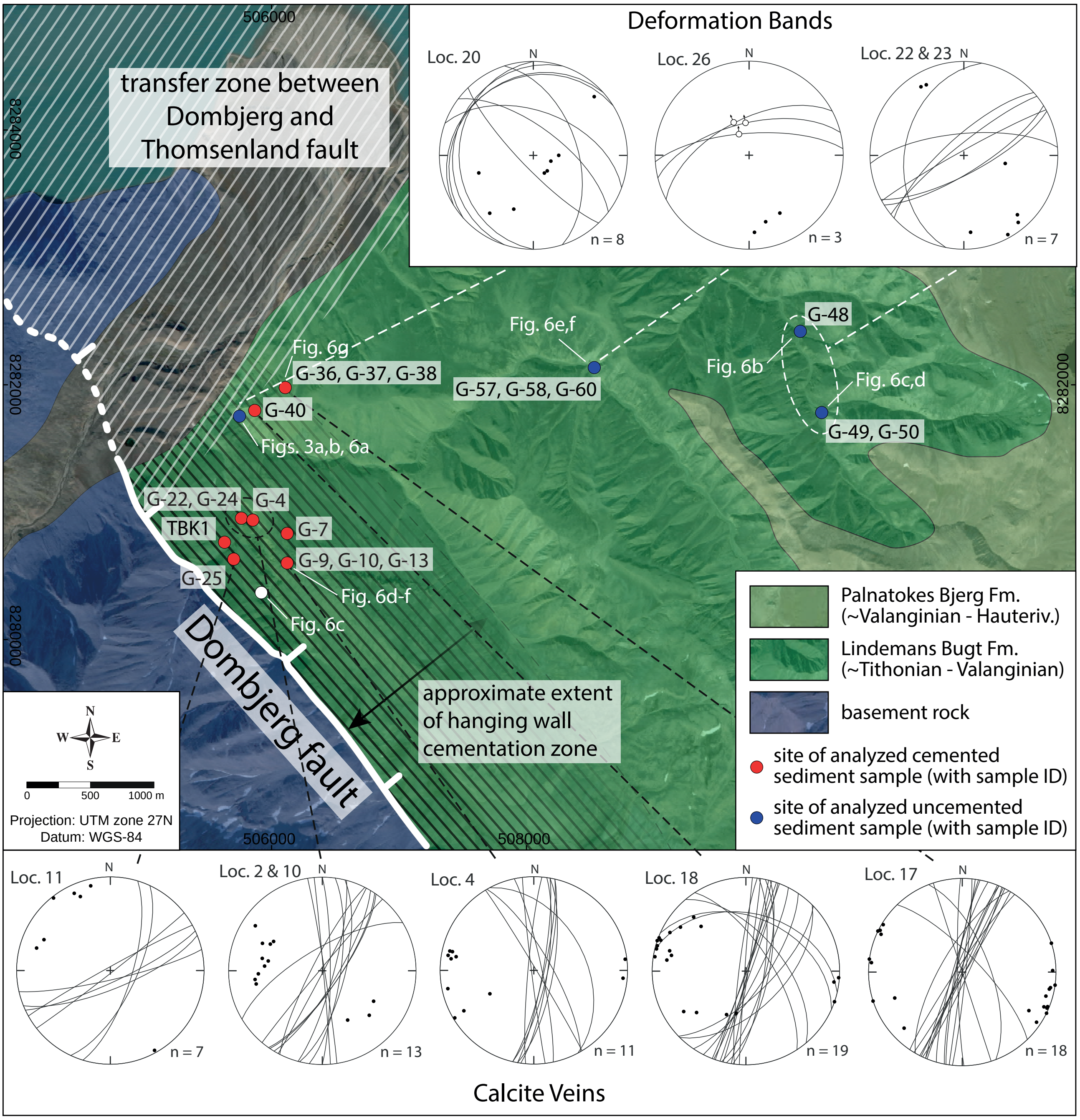

Figure 2: Geological map of study area with locations of outcrops and samples analyzed in this study. Inset of stereographic plot shows orientation of calcite veins / deformation bands in the respective outcrops. Sample coordinates provided in supplementary table S1. See Fig. 1b for location. Base satellite image from Google Earth / Digital Globe.

Figure 3: Field photos illustrating characteristics of veins and contact of cemented and uncemented sediments. (a,b) calcite cementation form lobes and appears to partially enclose uncemented sediments; (c) single sediment layers and lenses (light yellowish color) remain devoid of calcite cement in otherwise dominant calcite-cemented strata; (d) vein fill consisting of multiple generations of microcrystalline calcite (location of sample G-9 thin section marked with white frame); (e) calcite vein with a thin rim of microcystalline calcite (sample G-10 derives from this vein, though exact location not in picture); (f) vein consiting of a microcrystalline calcite rim and an infill of microcrystalline calcite and sediment grains (sample G-13 derives from this vein, though exact location not in picture); (g) microcrystalline calcite infill succeeded by elongate calcite growth in upper part of vein (location of sample G-37 thin section marked with white frame). See figure 2 for location of photos.

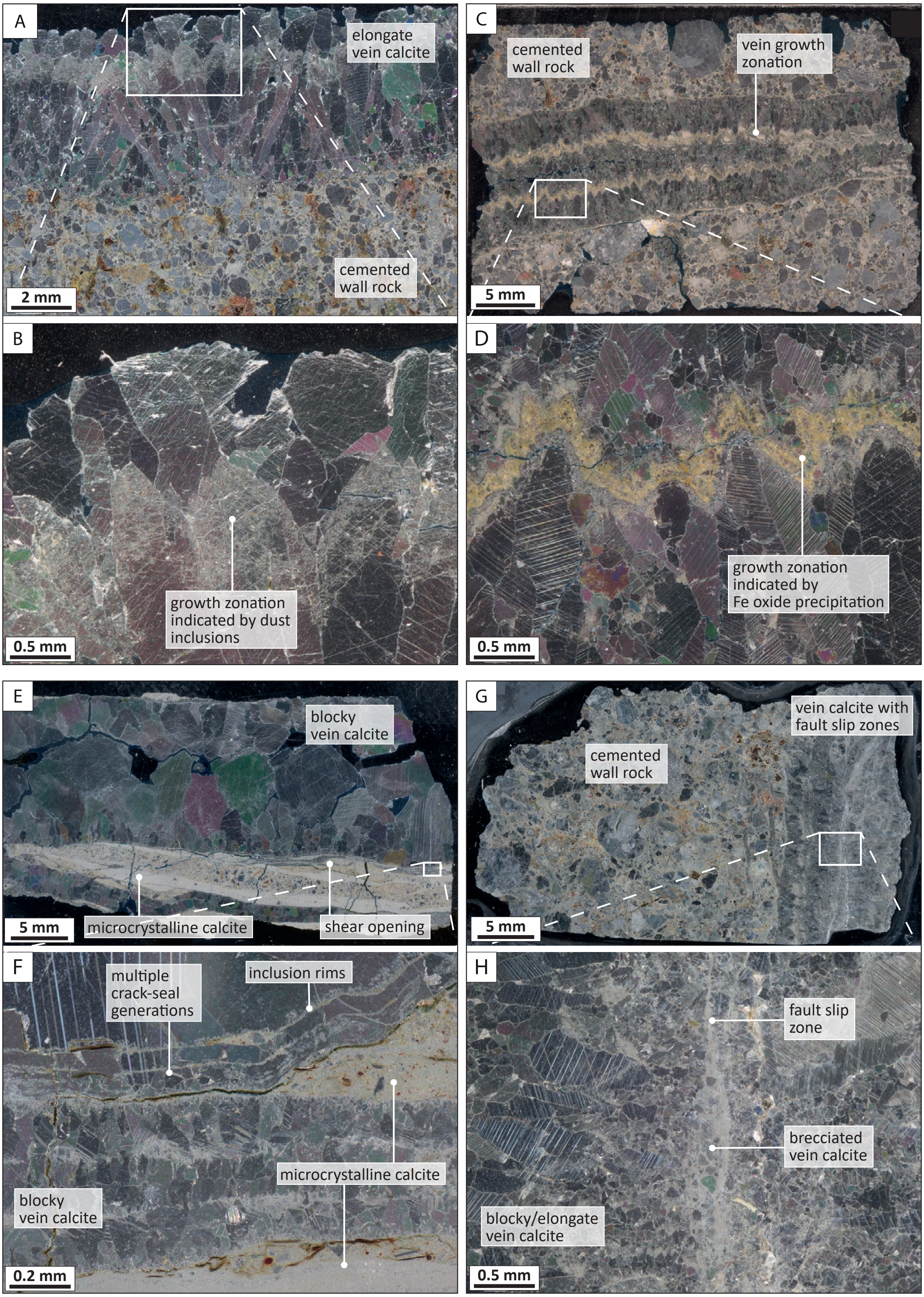

Figure 4: Thin section photos of calcite veins. (a,b) vein with growth generations that are distinguishable through the degree of dust inclusions; (c,d) vein exhibiting growth zonations with the inclusion of Fe-oxide precipitates; (e,f) vein exhibiting crack-seal texture with inclusion bands; light brownish material is microcystalline calcite (see chapter 4.2 and gure 5 for detailed explanations); (g,h) vein comprising multiple fault slip zones. All images taken in polarized incident ring light.

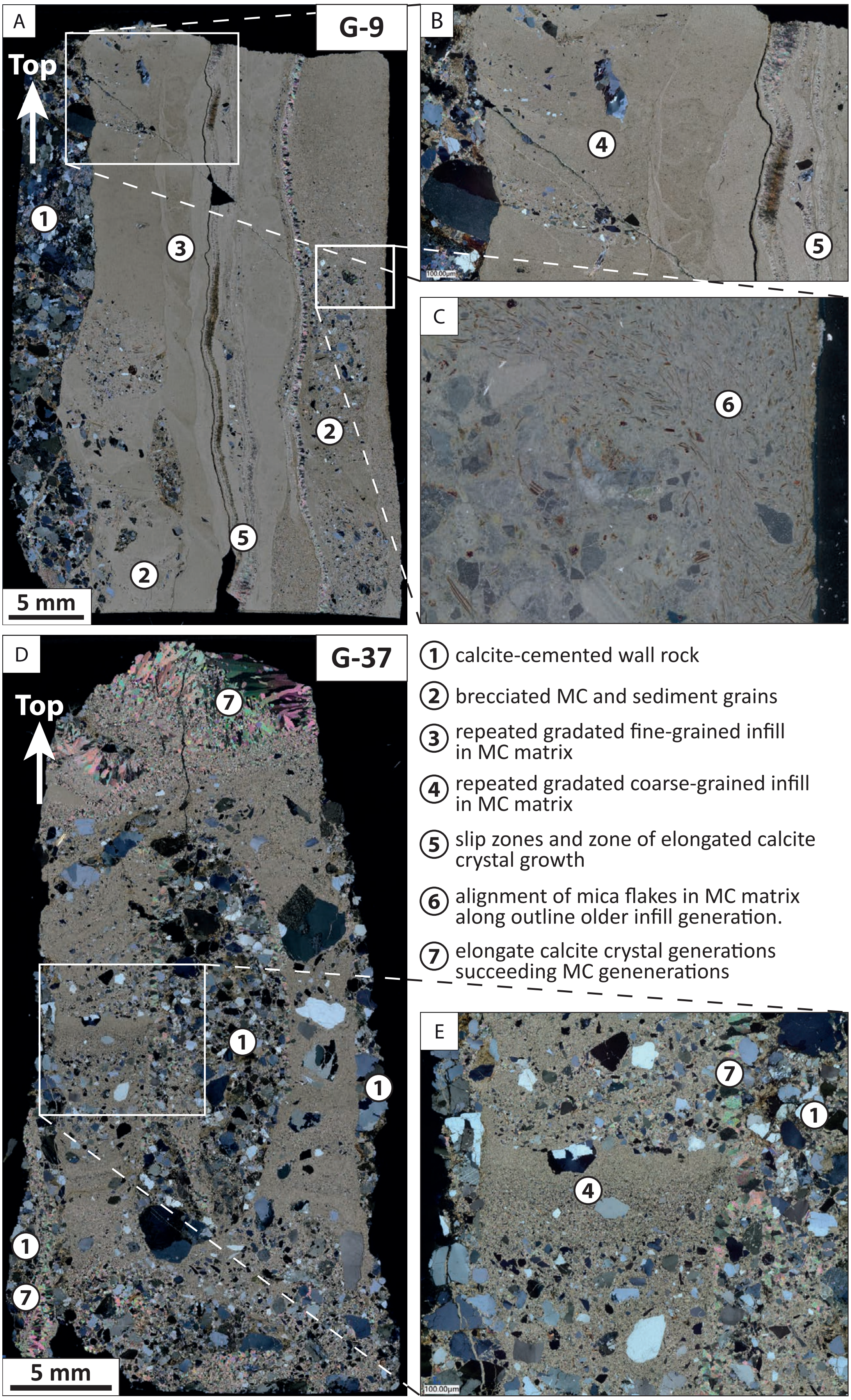

Figure 5: Thin section photos of three vein samples hosting microcystalline calcite (MC; light brownish mass in cross-polarized light) infill. (a-c) vertical face of sample G-9 shows an array of vein fill generations parallel to the wall rock. Within the generations a repeated gradation of upward fining infill is present. (d, e) vertical face of sample G-37 exhibits multiple generations of upward-fining vein fill, that are succeeded by elongate calcite crystal growth. (f) the horizontal face of sample G-13 shows a transition of vein fill from elongate calcite crystals to MC hosting lithic fragments. Main characteristics in thin sections are pointed out with numbers.

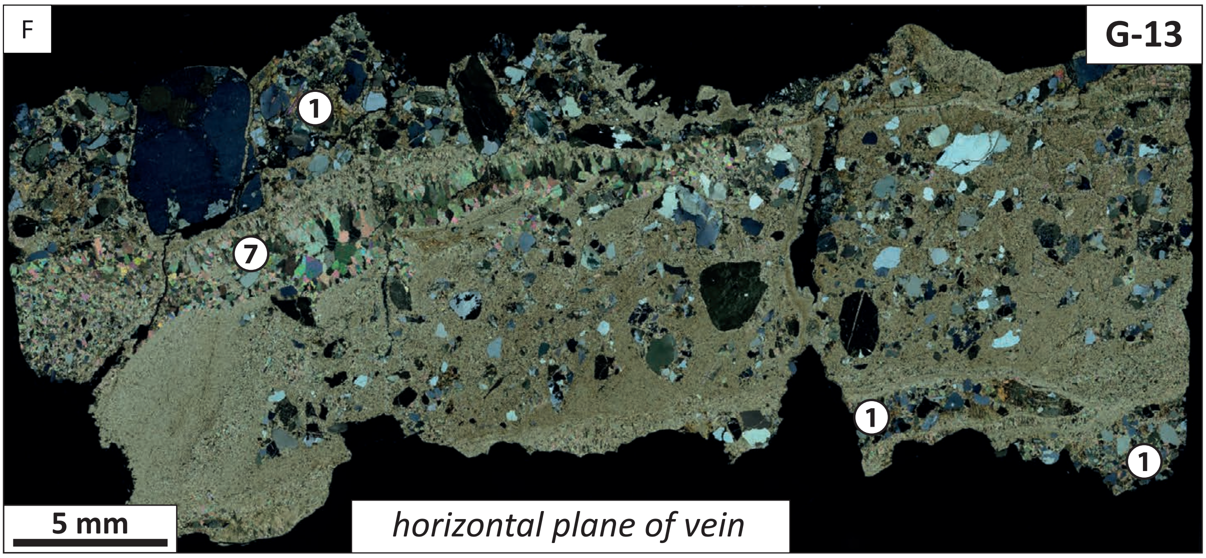

Figure 5: (continued).

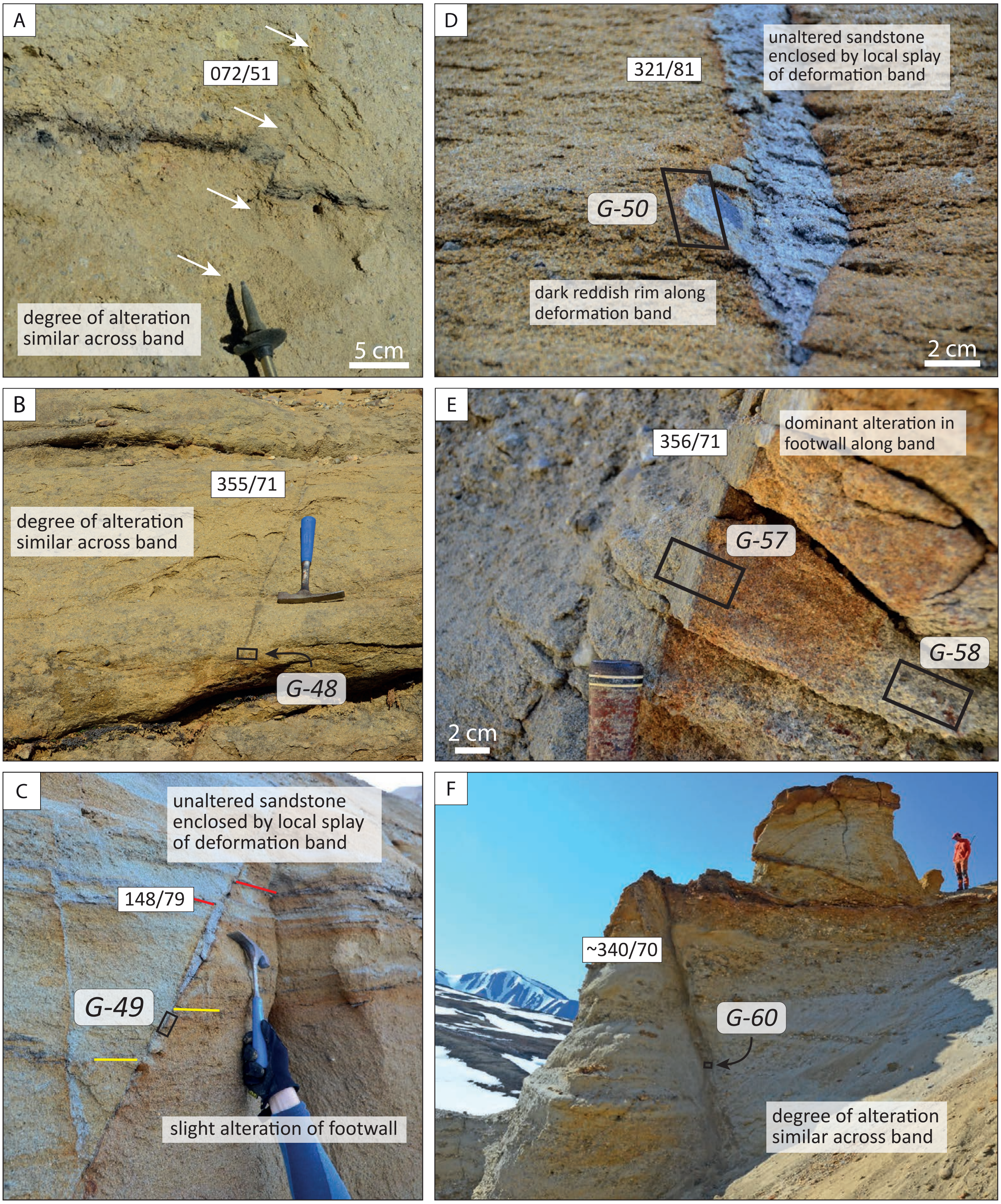

Figure 6: Field photos of deformation bands with orientation and sample position (where available). (a) deformation band offsetting a layer of organic material by ~3 cm normally (apparent reverse displacement is due to cutting effect; location 20). (b) deformation band with no visible offset (location 22). (c) deformation band with ~5 cm normal displacement and exhibiting a splay zone enclosing a section of unaltered host rock; note the preferred reddish alteration of the footwall (location 23). (d) deformation band splay enclosing unaltered host rock; note dark reddish rim along band in the otherwise yellowish host rock (location 23); (e) deformation band showcasing dominant footwall alteration, while hanging wall rock remains unaltered. (f) deformation band cluster that has merged to form a mature fault with an oset >5 m (i.e. larger than exposed vertical section). Note that structures in (e) and (f) are taken ~20 m apart from each other and derive from the same fault (location 26).

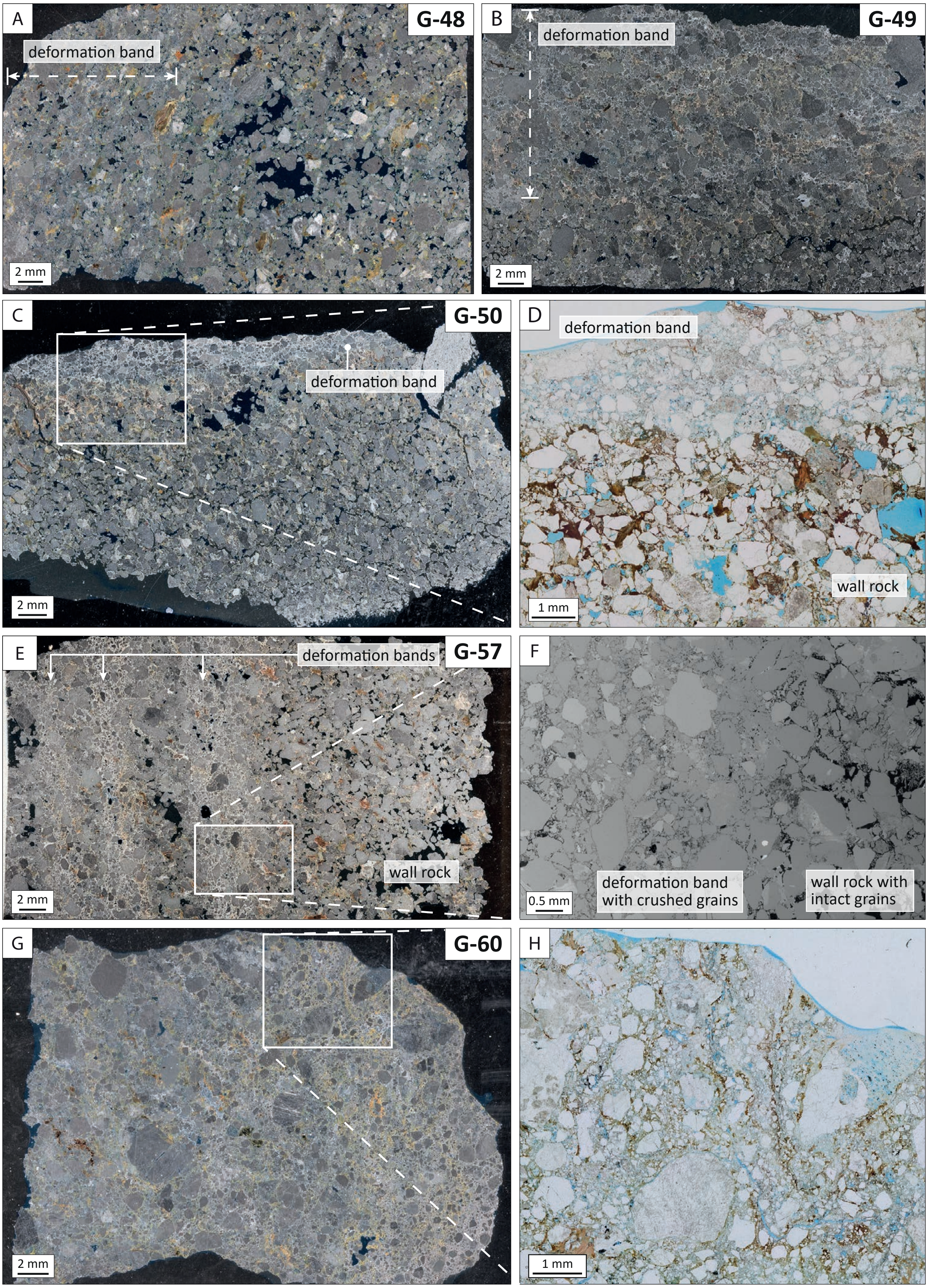

Figure 7: Thin section photos of deformation bands. (a,b) samples G-48 and G-49 comprise deformation bands with low degree of cataclasis and subtle boundary to wall rock. (c,d) sample G-50 with deformation band showing a distinct boundary to the wall rock indicated by the brownish coloration of the latter; (e,f) sample G-57 exhibiting an array of three deformation bands; (g,h) sample G-60, deriving from the core of a cataclastic zone (Fig. 6f) showing intense grain fracturing and cataclasis in the whole thin section. Images a,c,e,g are taken in poralized incident ring light; d,h in plane-polarized light; f in backscattered electron. Large pores in all images are due to grain plucking during thin section preparation. For locations of samples in the outcrop see figure 6.

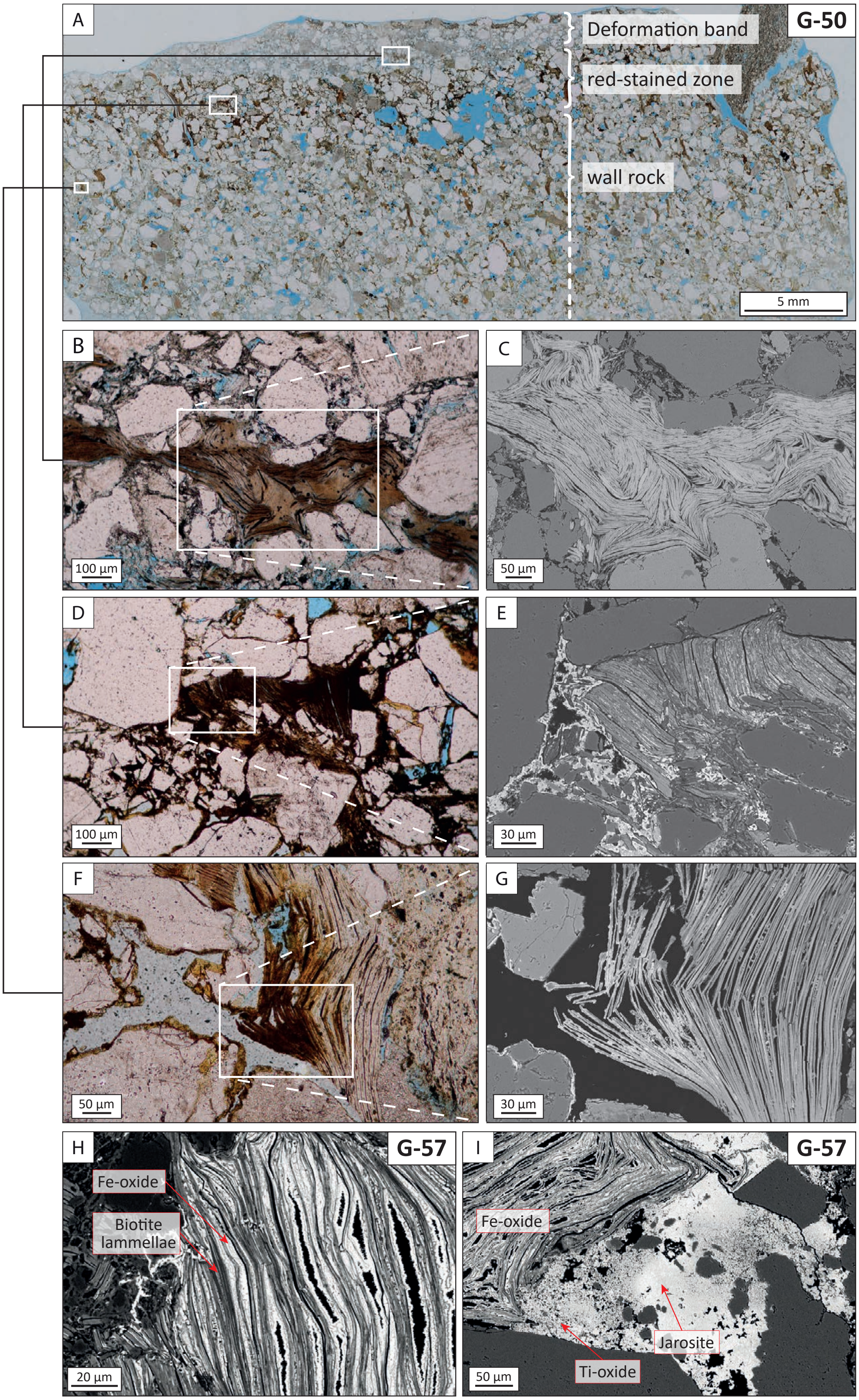

Figure 8: Thin section photos of deformation band and wall rock illustrating the degree of biotite alteration (a-g of sample G-50; h, i of sample G-57) in plane polarized light and backscatter electron imaging in and along the deformation band. (b,c) unaltered and intensively deformed biotite within deformation band; (d,e) altered and deformed and broken biotite lamellae with large quantity of Fe-oxides in red-stained zone; (f,g) slightly deformed biotite with alteration and oxide-precipitation restricted to delaminated part of biotite grain in wall rock; (h,i) intense Fe-, Ti-oxide, and jarosite precipitation within and near biotite grains in sample G-57 (EDX spectra and element maps in supplements S2).

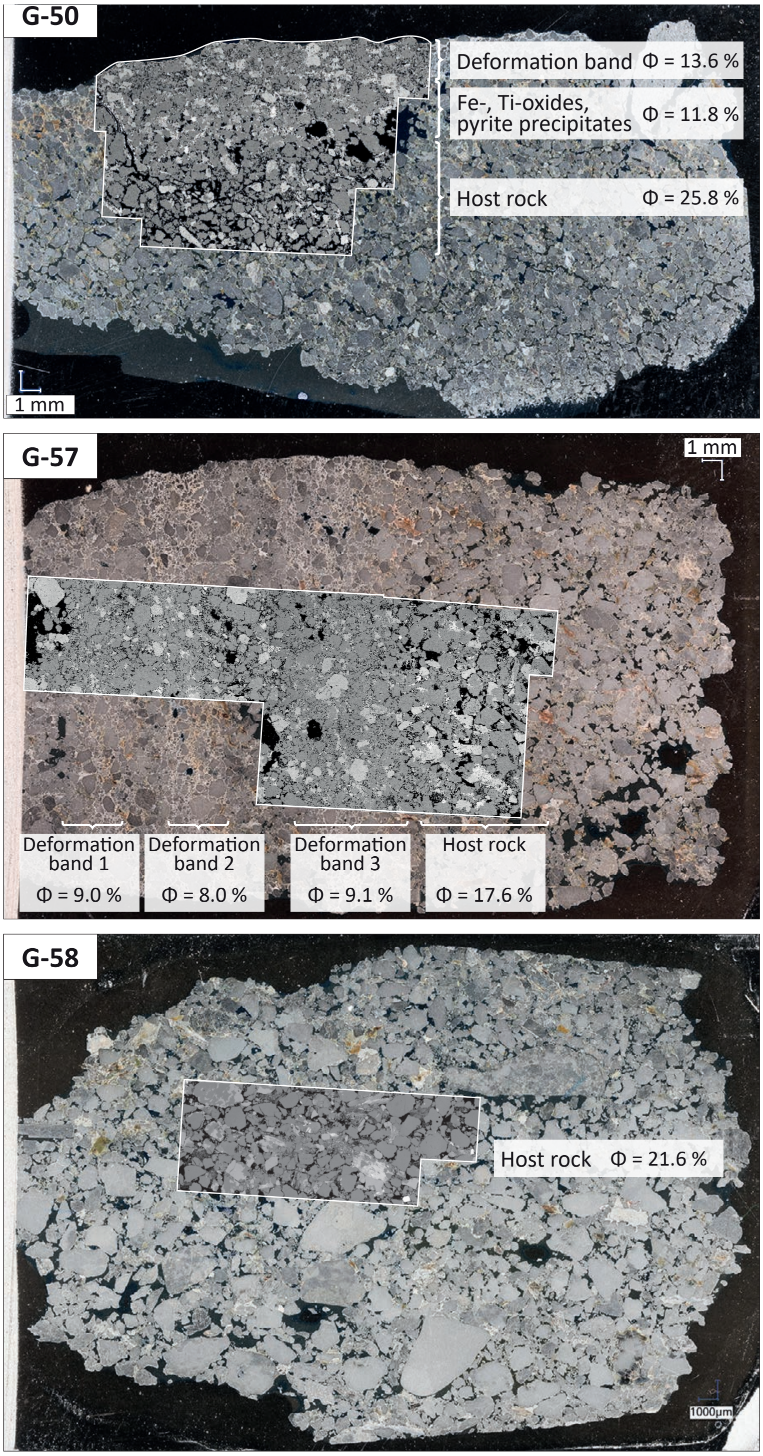

Figure 9: Thin section photos of deformation bands (sample G-50, G-57) and host rock (sample G-58) with respective porosity values. Notice the porosity reduction from host rock to bands resulting from the cataclastic grain crushing. Porosity reduction also occurs along the bands, due to preferential precipitation of Fe- / Ti- oxides and pyrite (sample G-50). Sample G-58 is taken ~20 cm away from sample G-57 and has a porosity slightly higher than the host rock of G-57. This is in agreement with field appearance with a decrease in red staining away from the cluster of deformation bands. Porosity derived from 2-D image analysis of backscatter electron images (inset overlays in images).

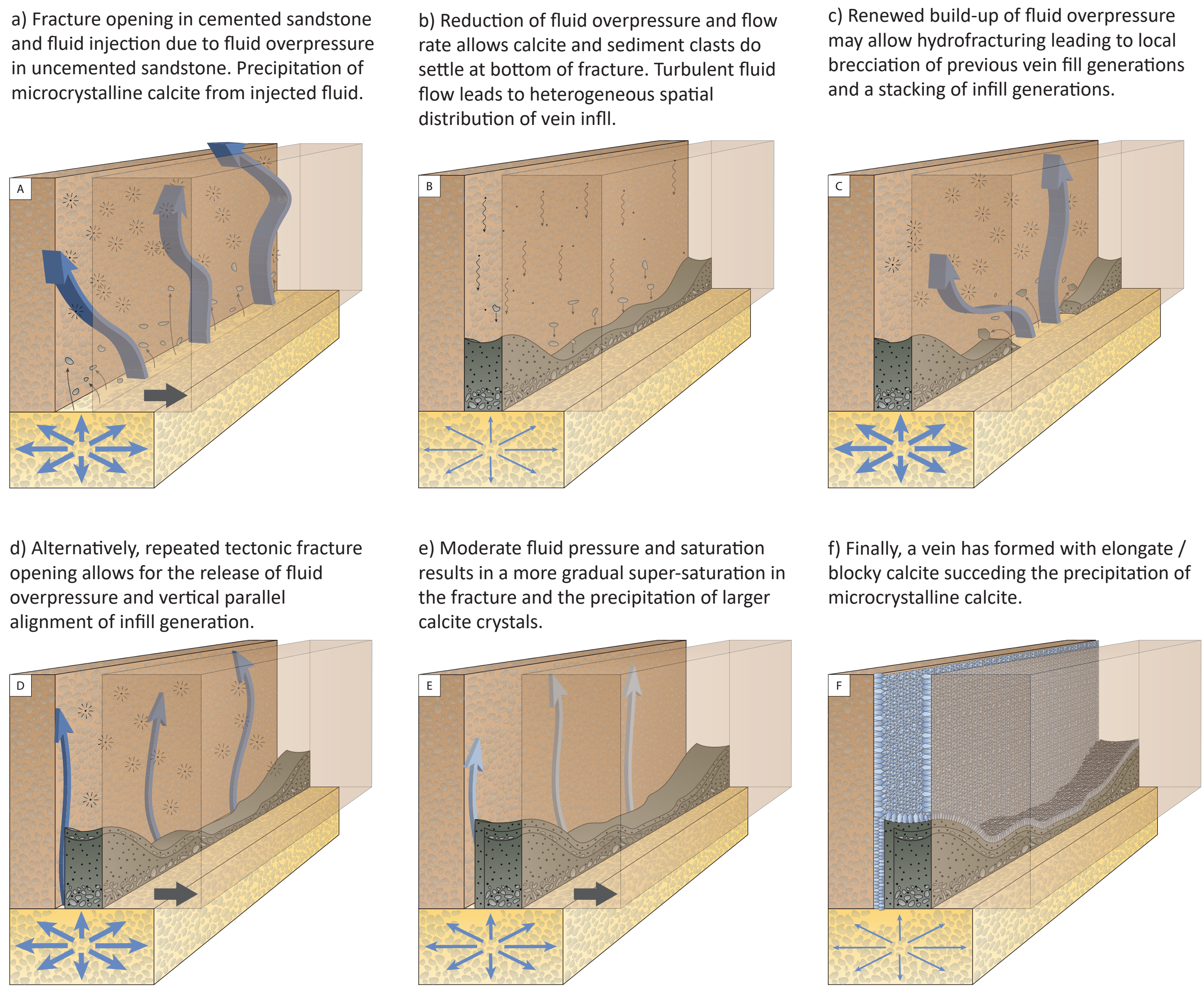

Figure 10: Conceptual model for the formation of microcrystalline calcite infill found in number of veins cuting through cemented sandstone within the cementation zone along the Dombjerg fault. The inferred main driver for the formation is initial calcite-saturated overpressured fluid in uncemented sandstone whose injection into a forming fracture is accompanied by sudden fluid pressure drop. This results in an instant supersaturation with respect to calcite and forces its quick precipitation.

Table 1: Porosity data of deformation band samples derived from BSE image analysis (cf. fig. 9).

Sample	**ϕ wall rock**	**ϕ def band**	**ϕ alteration zone**	**Def band width**	**displacement**
G-48	21.9	14.9	-	12.5 mm	0 cm
G-49	18.5	7.1	5.2	15.0 mm	5 cm
G-50	25.8*	13.6	11.8	1.5-3.0 mm	1-2 cm
G-57 / G-58	21.6	9.1 / 8.0 / 9.0	17.6	2-4 mm	n/a
G-60-2	-	8.8	-	> 250 mm	> 500 cm

* wall rock of G-50 suffered from expansion during impregnation.

Table S1: Sample localities.

Sample	Latitude	Longitude	type	Lithology / stratigraphic formation
G-4	74.617573°	-20.801874°	calcite vein	Lindemans Bugt Formation
G-7	74.616583°	-20.792948°	calcite vein	Lindemans Bugt Formation
G-9	74.614542°	-20.792949°	vein with microcrystalline calcite	Lindemans Bugt Formation
G-10	74.614542°	-20.792949°	vein with microcrystalline calcite	Lindemans Bugt Formation
G-13	74.614542°	-20.792949°	vein with microcrystalline calcite	Lindemans Bugt Formation
G-22	74.617714°	-20.805125°	calcite vein	Lindemans Bugt Formation
G-24	74.617714°	-20.805125°	calcite vein	Lindemans Bugt Formation
G-25	74.614824°	-20.807134°	calcite vein	Lindemans Bugt Formation
G-36	74.626854°	-20.793191°	calcite vein	Lindemans Bugt Formation
G-37	74.626854°	-20.793191°	vein with microcrystalline calcite	Lindemans Bugt Formation
G-38	74.626854°	-20.793191°	calcite vein	Lindemans Bugt Formation
G-40	74.625263°	-20.801344°	calcite vein	Lindemans Bugt Formation
G-48	74.630671°	-20.656902°	deformation band	Lindemans Bugt Formation
G-49	74.625113°	-20.652759°	deformation band	Lindemans Bugt Formation
G-50	74.625113°	-20.652759°	deformation band	Lindemans Bugt Formation
G-57	74.628168°	-20.711449°	deformation band	Lindemans Bugt Formation
G-58	74.628168°	-20.711449°	wall rock 10 cm away from deformation band	Lindemans Bugt Formation
G-60	74.628168°	-20.711449°	deformation band	Lindemans Bugt Formation
TBK1	74.615847°	-20.808716°	calcite vein	Lindemans Bugt Formation

Supplement S2: SEM EDX spectra and element maps of precipitates along biotite (c.f. figure 8i).

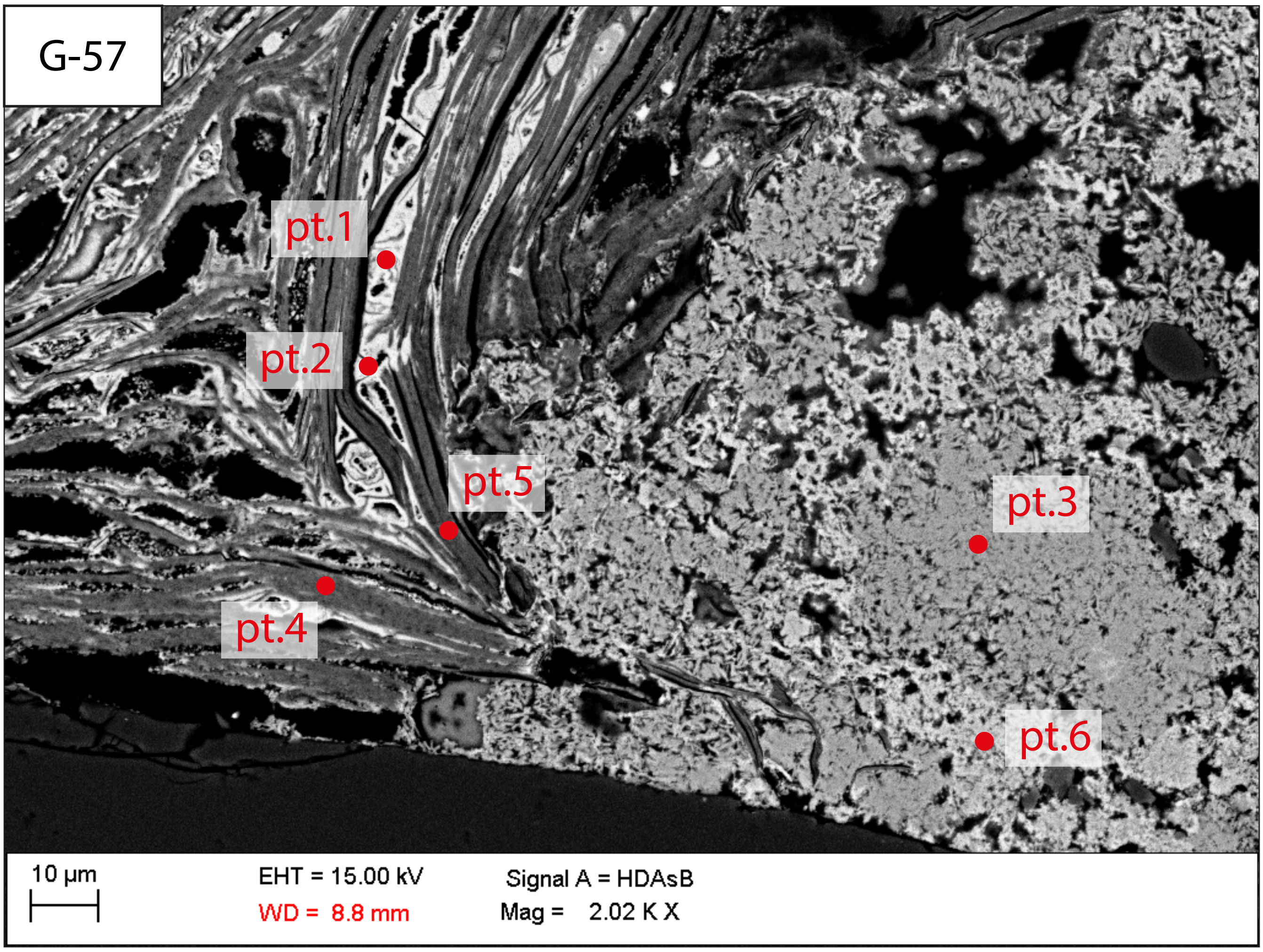

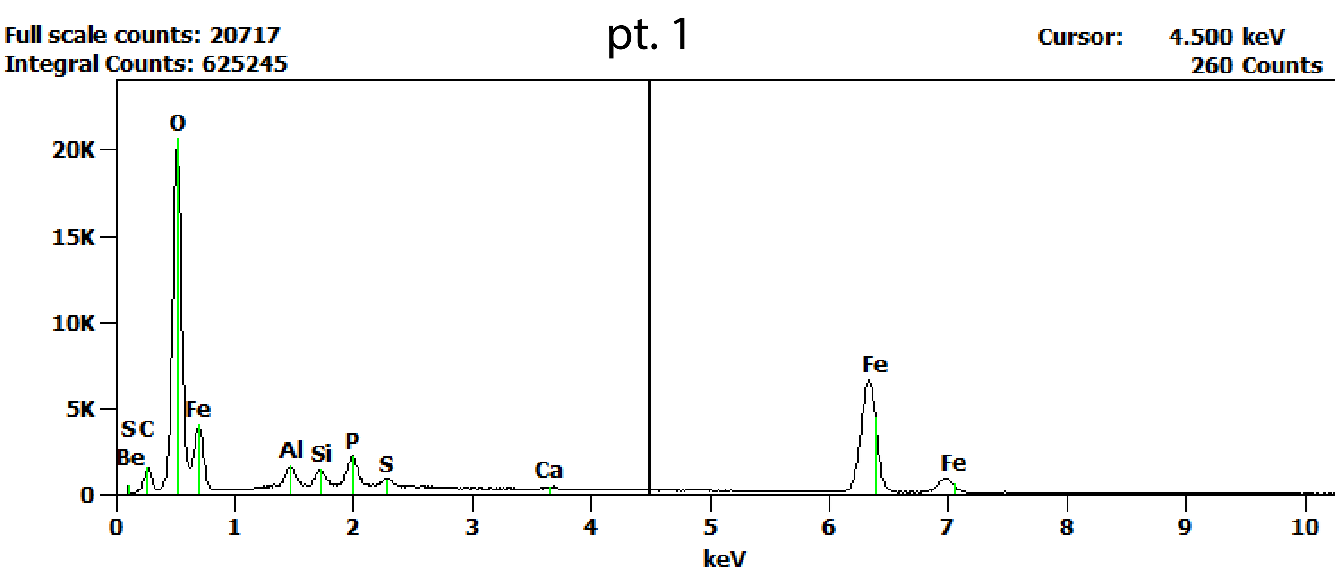

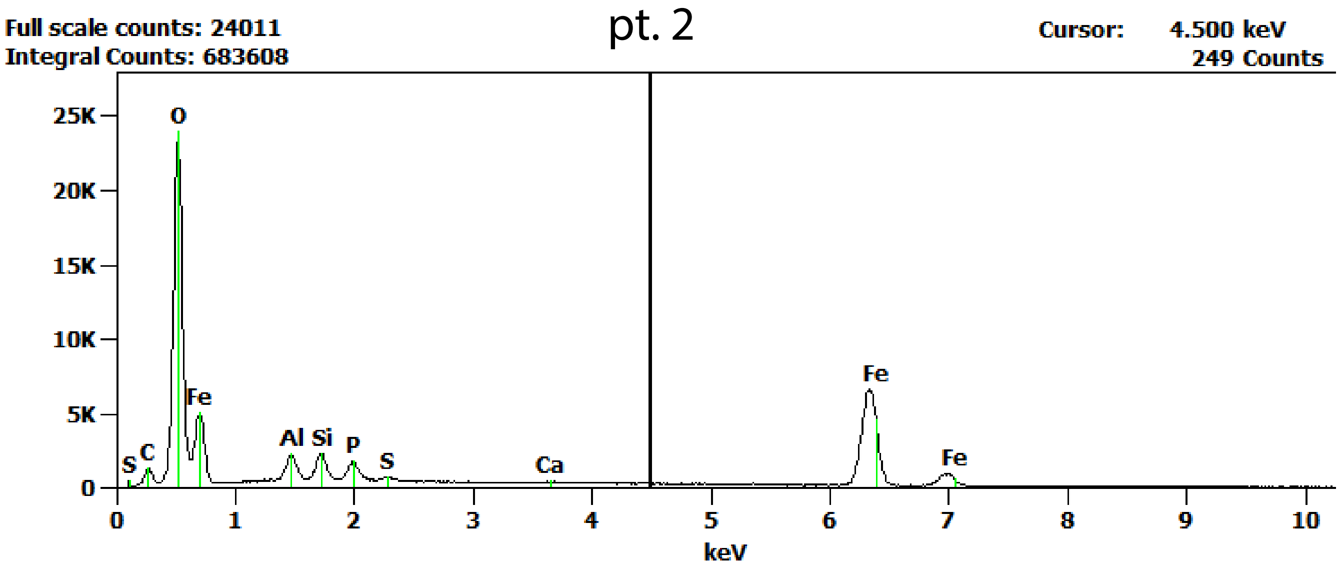
pt. 2
Full scale counts: 24011
Integral Counts: 683608
Cursor: 4.500 keV
249 Counts
25K
20K
15K
10K
5K
0
O
Fe
S
C
Al
Si
P
S
Ca
Fe
Fe
0
1
2
3
4
5
6
7
8
9
10
keV

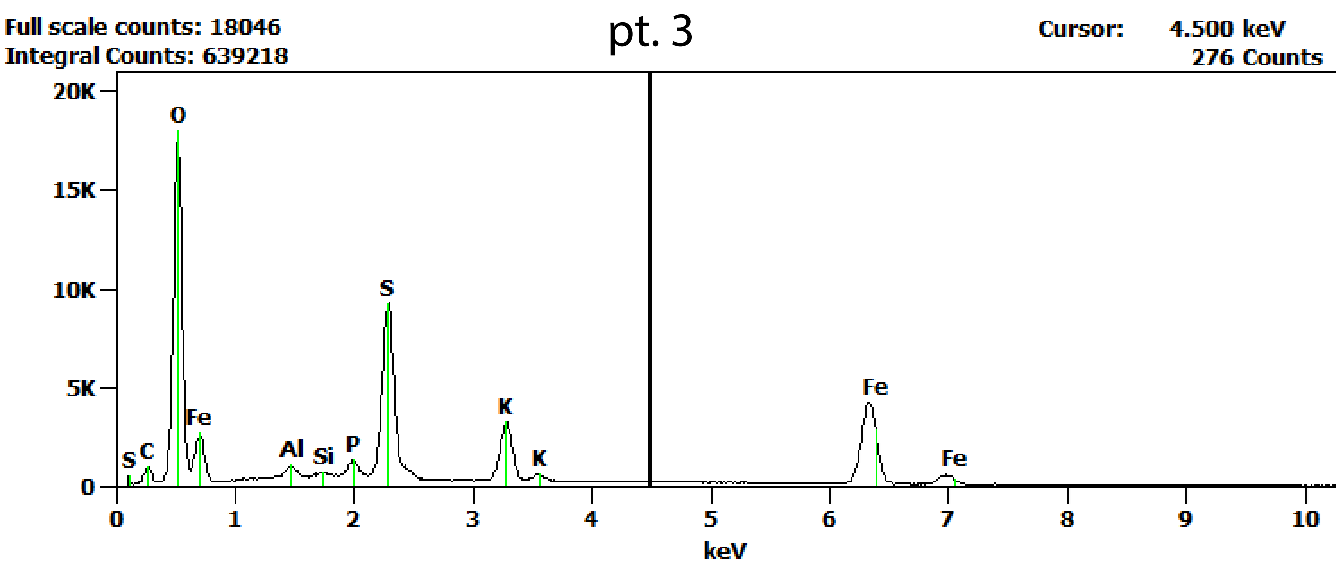
pt. 3
Full scale counts: 18046
Integral Counts: 639218
Cursor: 4.500 keV
276 Counts
20K
15K
10K
5K
0
O
S
Fe
S
C
Al
Si
P
K
K
Fe
Fe
0
1
2
3
4
5
6
7
8
9
10
keV

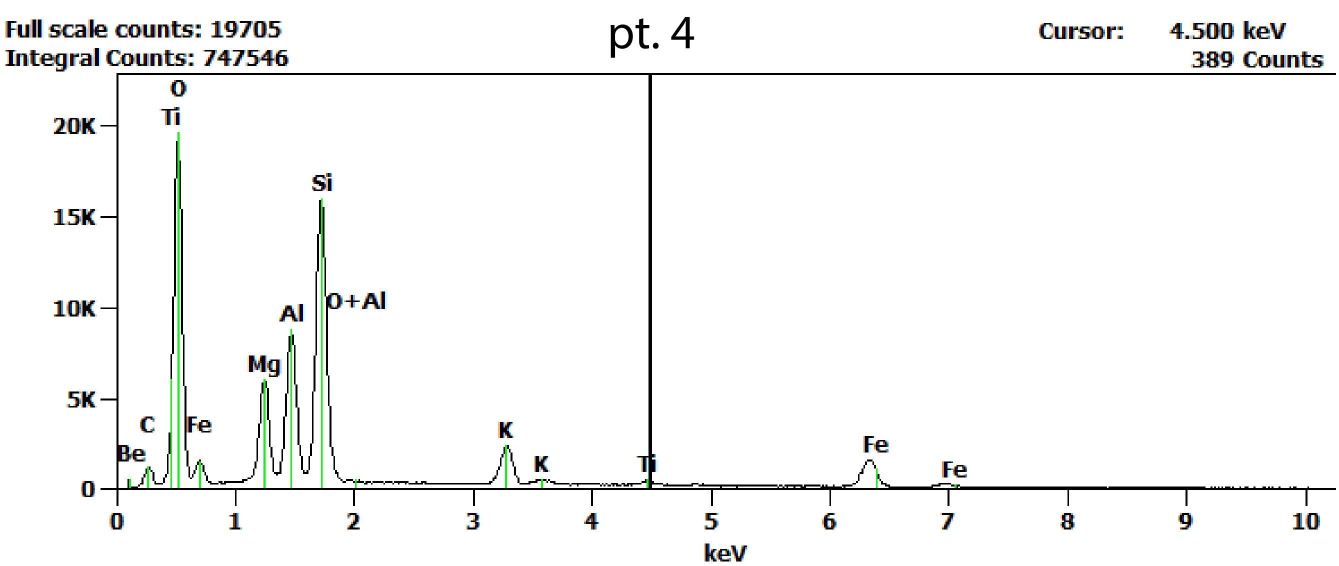
pt. 4
Full scale counts: 19705
Integral Counts: 747546
Cursor: 4.500 keV
389 Counts
20K
15K
10K
5K
0
O
Ti
Si
O+Al
Al
Mg
C
Fe
Be
K
K
Ti
Fe
Fe
0
1
2
3
4
5
6
7
8
9
10
keV

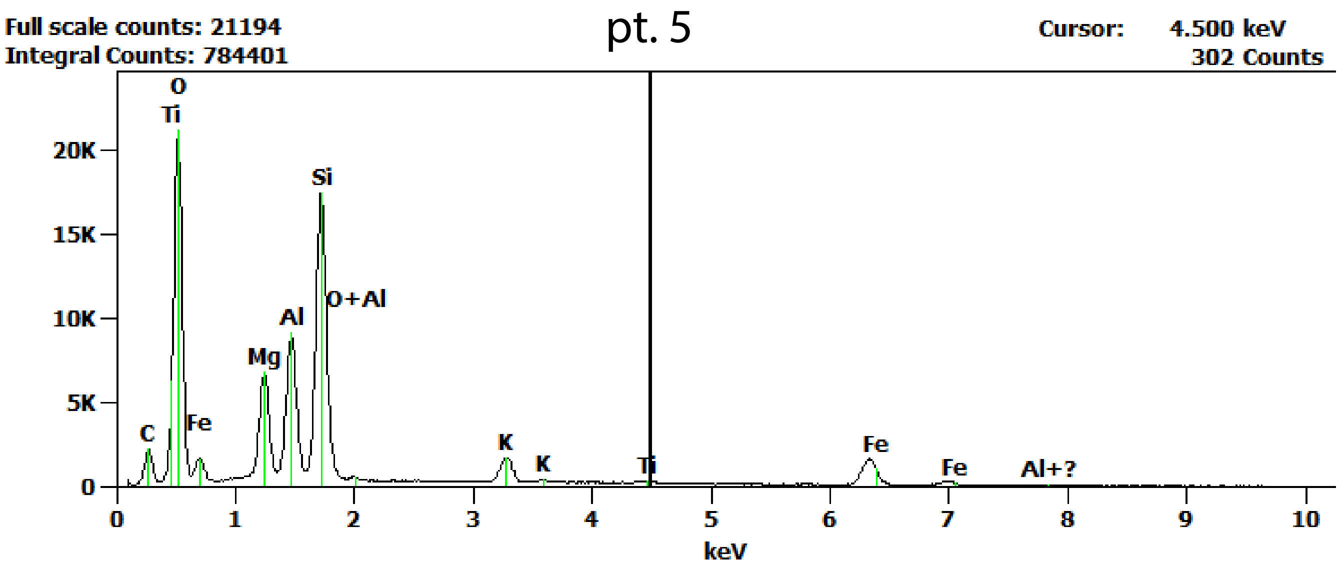
Full scale counts: 21194
Integral Counts: 784401
pt. 5
Cursor: 4.500 keV
302 Counts
O
Ti
Si
O+Al
Al
Mg
C
Fe
K
K
Ti
Fe
Fe
Al+?
20K
15K
10K
5K
0
0
1
2
3
4
5
6
7
8
9
10
keV

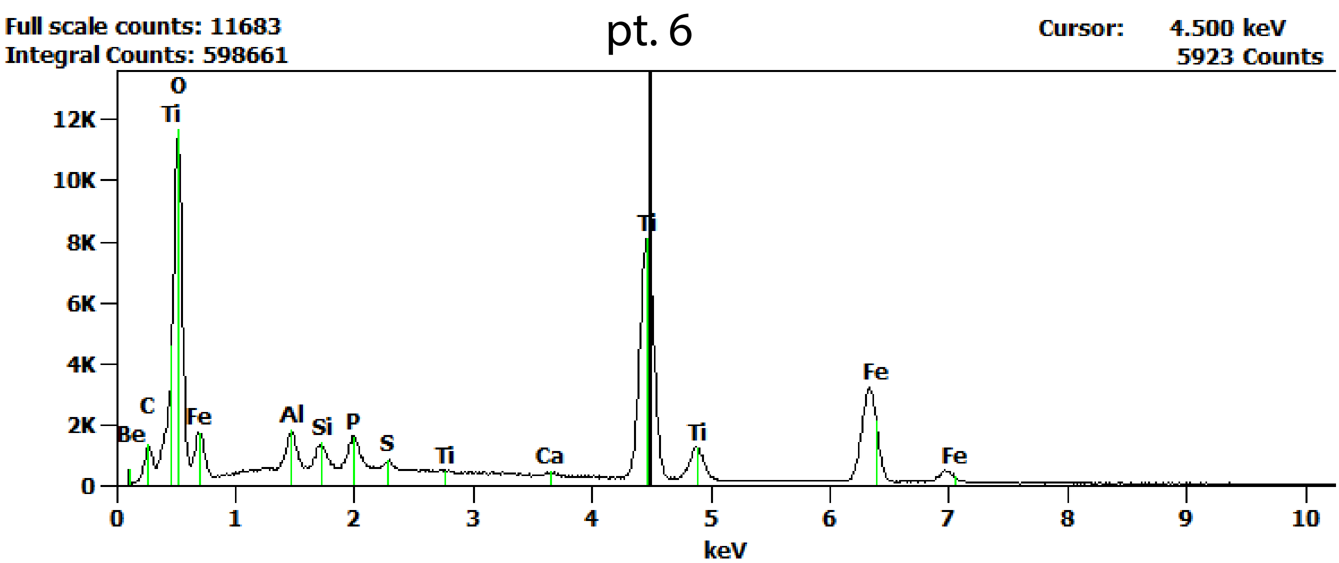
Full scale counts: 11683
Integral Counts: 598661
pt. 6
Cursor: 4.500 keV
5923 Counts
O
Ti
Ti
Fe
C
Be
Fe
Al
Si
P
S
Ti
Ca
Ti
Fe
12K
10K
8K
6K
4K
2K
0
0
1
2
3
4
5
6
7
8
9
10
keV

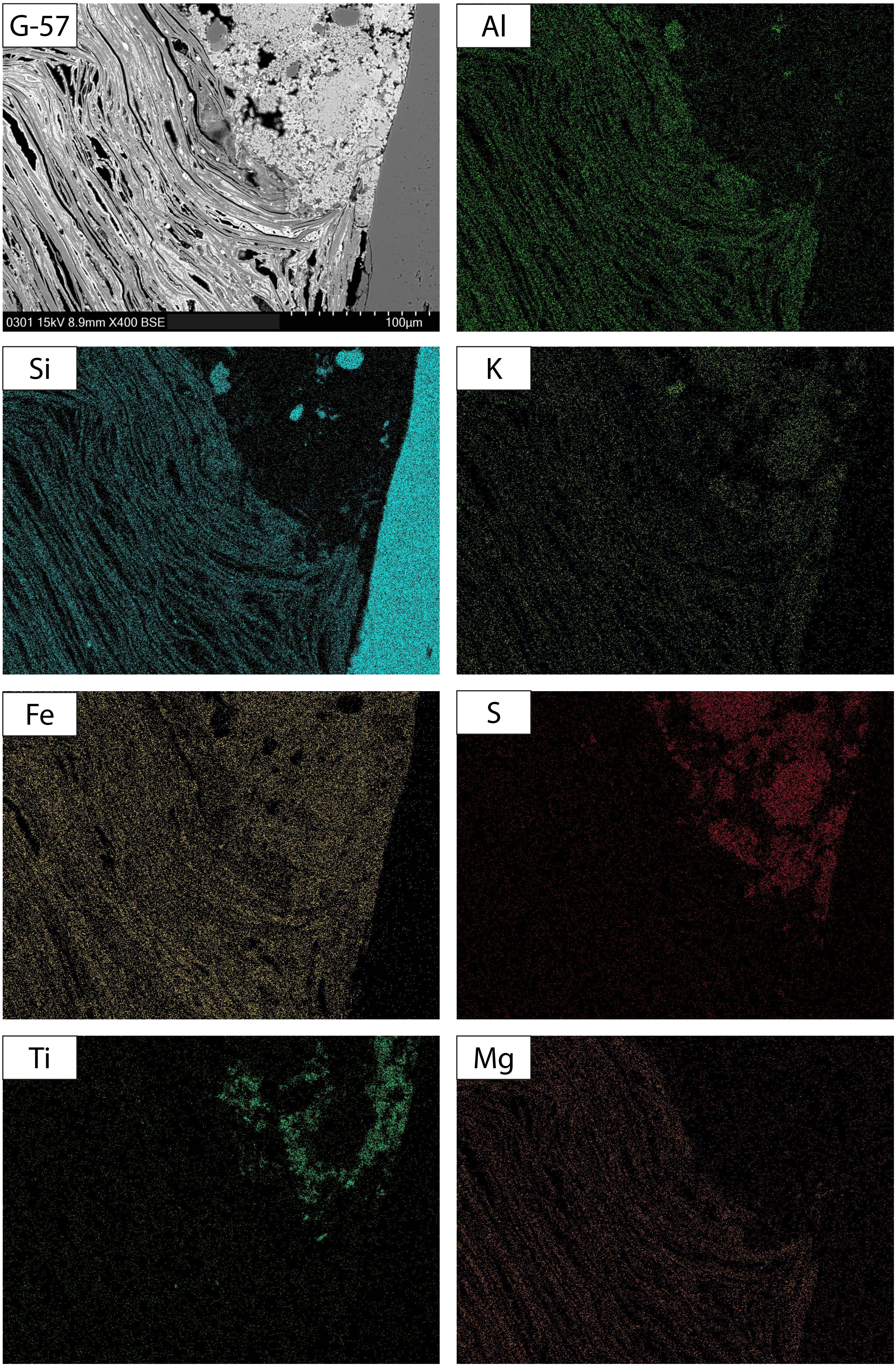
G-57
0301 15kV 8.9mm X400 BSE
100µm
Al
Si
K
Fe
S
Ti
Mg